



## Statistical representative elementary area of shale inferred by micromechanics

Philippe Cosenza, Anne-Laure Fauchille, Dimitri Prêt, Stephen Hedan, Albert  
Giraud

### ► To cite this version:

Philippe Cosenza, Anne-Laure Fauchille, Dimitri Prêt, Stephen Hedan, Albert Giraud. Statistical representative elementary area of shale inferred by micromechanics. *International Journal of Engineering Science*, 2019, 142, pp.53 - 73. 10.1016/j.ijengsci.2019.05.012 . hal-03485826

**HAL Id: hal-03485826**

**<https://hal.science/hal-03485826>**

Submitted on 20 Dec 2021

**HAL** is a multi-disciplinary open access archive for the deposit and dissemination of scientific research documents, whether they are published or not. The documents may come from teaching and research institutions in France or abroad, or from public or private research centers.

L'archive ouverte pluridisciplinaire **HAL**, est destinée au dépôt et à la diffusion de documents scientifiques de niveau recherche, publiés ou non, émanant des établissements d'enseignement et de recherche français ou étrangers, des laboratoires publics ou privés.



Distributed under a Creative Commons Attribution - NonCommercial 4.0 International License

1  
2  
3  
4  
5  
6  
7  
8  
9  
10  
11  
12  
13  
14  
15  
16  
17  
18  
19  
20  
21  
22

**Statistical Representative Elementary Area of Shale Inferred by  
Micromechanics**

*Intended for publication in International Journal of Engineering Science*

## Abstract

This paper provides new estimates for the Representative Elementary Area (REA) sizes of the following two shales that are actively being studied in the framework of deep disposal of radioactive waste: Callovo-Oxfordian (COx) claystone from the Meuse/Haute-Marne underground research laboratory (Eastern France) and Toarcian argillite from the experimental station of Tournemire (Southern France). The REA sizes, named  $L_{REA}$ , were obtained from two mineral maps following the classic “counting box” (CB) method and a statistical approach that introduces the concept of a “statistical” REA. Following this approach, a “statistical” REA is related not only to the microstructure and the properties of each of the components but, above all, to a given precision in the estimation of the effective property depending on the number of realizations that one is ready to generate. The probabilistic concept of realization is here, from a practical viewpoint, a subdomain of a mineral map in which the apparent morphological or mechanical properties have to be calculated. In this study, the apparent elastic moduli of the subdomain have been estimated using two micromechanical models. The first micromechanical model consisted of an inclusion-based model for which spherical nonclay grain is embedded in a clay matrix in which the values of its transverse isotropic stiffness tensor have been taken from literature. The second micromechanical model was an isotropic inclusion-based model for which a spherical nonclay grain is embedded in a clay matrix; the elastic moduli values have been inverted by a Monte-Carlo approach from the engineering moduli of both shales under study. Our calculations have shown the following results: (i) the statistical morphological  $L_{REA}$  considering the surface clay fraction are of the same order of magnitude as those measured in other shales and those obtained by the simple CB method, with relative error values between 5 and 10%, (ii) the mechanical  $L_{REA}$  values associated with the bulk modulus and shear modulus are significantly greater than that of the morphological  $L_{REA}$ , and (iii) the mechanical  $L_{REA}$  estimates of the shear modulus are greater than that of the

bulk modulus. Moreover, our study highlights that these qualitative results do not depend on the chosen micromechanical models and, thus, would be independent of the underlying anisotropic nature of shale.

**Keywords:** microstructure, shales, clay-rocks, anisotropy, clay, elastic properties.

**Short title:** Mechanical REA of shales inferred by micromechanics.

#### **Highlights**

- New estimates for the REA sizes of COx claystone and Tournemire argillite.
- Mechanical REA size is greater than morphological REA size.
- REA sizes of Tournemire argillite are greater than those of the COx map.
- REA sizes of shear modulus are greater than those of the bulk modulus.
- These results do not depend on the chosen micromechanical models.

## 1. Introduction

Clay rocks, often called shales, are being studied as potential host rocks for high-level radioactive waste repositories in several industrial countries (e.g., ANDRA, 2005; Pusch, 2006) and form the main geological caps of many hydrocarbon reservoirs (e.g., Aplin and Larter, 2005). Organic-rich clay rocks are considered to be the key petroleum source rocks for the coming decades (e.g., Klaver et al., 2015). These geological formations are highly heterogeneous at multiple scales, but a major proportion of the literature agrees that the following relevant microstructural levels must be considered (e.g., Bennett et al., 1991; Jakobsen et al., 2003; Ulm et al., 2005; Ortega et al. 2007; 2009; Bobko and Ulm, 2008; Loucks et al., 2012; Cariou et al., 2013; Keller, 2015) (Figure 1):

- Level 0 is the scale of elementary clay layers.
- Level 1 is the scale for which the elementary clay layers are packed together to form clay particles.
- Level 2 is the submicrometer scale, often called the “microscopic” scale of porous clay composites constituted in a mixture of clay particles or aggregates.
- Level 3, often called the “mesoscopic” scale in geosciences, is the scale where the characteristic size is in the submillimeter range. At this scale, the rock is considered to be a porous clay matrix mixed with a population of nonclayey grains (mainly quartz, carbonates and pyrite). This is the scale of the mineral maps used in this work.
- Level 4 is a lamina type that is associated with an alternation of clay-rich layers and non-clayey materials (mainly quartz and carbonates).

With regards to the complexity of this hierarchical organization, the prediction of the engineering properties of shale from its microstructure is clearly a challenging task. In the following work, we will focus on the mesoscopic scale for which numerous theoretical studies

86 have been devoted to the calculations of the engineering or effective properties (e.g., Jakobsen  
87 et al., 2003; Levin and Markov, 2005; Ulm et al., 2005; Giraud et al., 2007a, 2007b; Ortega et  
88 al. 2007; 2009; Cariou et al., 2013; Cosenza et al., 2015a,b). This mesoscopic scale is often  
89 considered the key scale for modeling the mechanical and transport behaviors of clay rocks  
90 involved in high-level radioactive waste repositories (Abou-Chakra Guéry et al., 2010; Robinet  
91 et al., 2007; 2012; Cariou et al., 2013). These effective properties, which are inferred by  
92 numerical upscaling techniques or by homogenization theories, are used as inputs for numerical  
93 codes, often based on the finite elements method, for engineering purpose.

94 All the upscaling or homogenization approaches used to estimate these effective  
95 properties are based on the paramount concept of the Representative Elementary Volume  
96 (REV), which is required to “separate” the following two space scales: the scale of  
97 heterogeneity, i.e., nonclayey grains (or rigid inclusions) in our case, and the scale of  
98 engineering for which clay rock is viewed as a continuum of homogeneous medium. Thus, the  
99 REV is usually considered as a volume of heterogeneous material that is sufficiently large to  
100 be statistically representative of the rock, i.e., to include a relevant sampling of all the  
101 microstructural heterogeneities existing in the rock at the scale of interest (here, the mesoscopic  
102 scale) (e.g., Kanit et al., 2003; Zhang et al., 2017). At the same time, the REV has to be small  
103 enough, compared to the scale of the macroscopic geotechnical systems of study, “so that it  
104 may be considered as infinitesimal in the mathematical treatment” (Biot, 1941).

105 To our knowledge, the approaches used to estimate the size of a REV, named hereafter  
106  $L_{REV}$ , can be divided for the sake of simplicity into two groups that introduce the probabilistic  
107 concept of realization; here, a realization is any representation of the microstructure considered  
108 with a given size and a given fraction of heterogeneities. The first approach or group of  
109 approaches aims at using statistical parameters, e.g., mean, standard deviation or covariance, of  
110 a given geometrical or physical property (e.g., porosity, fraction of a given mineralogical phase,

mechanical property, etc.) calculated over a significantly large set of realizations to quantitatively describe the heterogeneous structure of the material of interest (Torquato and Stell, 1982; Zhang et al., 2000; Kameda et al., 2006; Houben et al. 2014; Klaver et al., 2015; Fauchille et al., 2018). Following these approaches, REV is defined as the elementary volume below which the property of interest varies significantly across the scale. Among these approaches, the “counting box” method and the covariance or the two-point probability function are likely the most popular and have been recently applied to 2D images acquired on shale samples (i.e., Pasidonia shale, Germany, Klaver et al., 2015; Callovo-Oxfordian argillites, France, Song et al., 2015; Opalinus clay, Switzerland, Keller et al., 2013; Houben et al. 2014; Bakken shale, United States of America, Liu and Ostadhassan, 2017; and Bowland shale, United Kingdom, Fauchille et al., 2018). It should be noted that most of these works have been performed on 2D images and, thus, provided estimations of the Elementary Representative Area (REA) size, hereafter named  $L_{REA}$ .

This first group of approaches is often referred to as “deterministic” approaches (Rolland du Roscoat, et al., 2007; Khdir et al., 2012), in contrast with a second group of approaches that explicitly introduce the concept of the “statistical” REV. Following Kanit et al. (2003) and Jeulin et al. (2004), a “statistical” REV is related not only to the microstructure and the physical properties of each components but, above all, to a given precision in the estimation of the effective property depending on the number of realizations “that one is ready to generate” (Jeulin et al., 2004). Consequently, in comparison with the aforementioned approaches, the “statistical”  $L_{REV}$  depends explicitly on an additional parameter, i.e., the precision desired for the estimate of the effective property and reached for a given number of realizations. Consequently, the estimate of the “statistical”  $L_{REV}$  cannot be unique without any associated precision and number of realizations. This statistical approach has been recently applied to

Opalinus clay samples taken from the Mont Terri rock laboratory in Switzerland (Houben et al., 2014; Keller, 2015; 2016a,b).

In summary, this brief review shows that a large variety of methods used to infer  $L_{REV}$  or  $L_{REA}$  estimates with regard to shale exist, and these estimates concern mainly the petrographical or mineralogical parameters of the porosity and mineral phases. Most of them have been obtained by deterministic approaches, e.g., the counting box method and dispersion method based on the standard deviation calculations. Moreover, to our knowledge, estimates of the mechanical  $L_{REV}/L_{REA}$  of shales are very scarce; one recent and single work was performed on Opalinus clay by Keller (2016a,b), and it focused on the dynamic elastic moduli.

The objective of this paper is thus twofold. First, we would like to provide new estimates of  $L_{REA}$  obtained from two mineral maps (Jorand, 2006; Fauchille, 2015) acquired from two shales extensively studied in the framework of the deep disposal of radioactive waste, as follows: Callovo-Oxfordian (COx) claystone from the Meuse/Haute-Marne underground research laboratory (Eastern France) and Toarcian argillite from the experimental station of Tournemire (Southern France). These estimates have been obtained by the classical counting box method and the statistical approach promoted by Kanit et al. (2003; 2006) and Jeulin et al. (2004). Second, we would like to quantify the statistical mechanical  $L_{REA}$  of COx claystone and Tournemire argillites by focusing on static elastic parameters for further engineering purposes. These mechanical  $L_{REA}$  are inferred by using micromechanical approaches, one of which implicitly accounts for the transverse isotropic nature of shale.

## **2. Mineral maps**

The  $L_{REA}$  estimates calculated in this study have been obtained from two mineral maps acquired following the methodologies described below.

The first mineral map, hereafter called the COx map, has been made from a sample taken from the Callovo-Oxfordian (COx) claystone, which is under extensive study at the



Meuse/Haute-Marne Underground Research Laboratory (MHM-URL) (Eastern France). The thickness of this formation is 130 m and its age is 150-160 My; the formation is located 420-550 m below the surface, in the eastern part of the Paris Basin (Andra, 2005). The Callovo-Oxfordian formation contains mainly 25 to 65 wt.% clay minerals, with 20-42 wt.% carbonates (calcite, dolomite, ankerite) and 15-31 wt.% quartz and feldspars (Andra, 2005). Considering nonclay minerals, feldspars contents are negligible regardless to quartz. Among carbonates, siderite and dolomite are negligible regardless to calcite. Thus, quartz and calcite will be the only nonclay minerals considered in the following.

This mineral map was prepared from a drill-core, denoted as EST05-709 (-492.2 m) and extracted from the Andra EST205 borehole (Jorand, 2006; Conil et al., 2018). It was obtained at a micrometer spatial resolution from an advanced image processing of a chemical elements map that was acquired through the use of a Cameca SX100 electron probe microanalyzer (Prêt, 2003). This electron microanalyzer provides quantitative concentration maps of 14 chemical elements (Al, Na, K, Ca, Si, Mg, Ti, Fe, S, Ba, Zr, P, Zn, Sr) on a 3 x 0.5 mm<sup>2</sup> area with a spatial resolution of 2 µm/pixel. The image processing of these maps is based on mineral thresholding methods that accommodate mixtures and solid solutions. For details, the reader is referred to Prêt (2003) and Prêt *et al.* (2010a,b). In our case, this methodology allows for the spatial location of 16 different minerals, including the following three different clay minerals: illite-smectite mixed layers, kaolinite and chlorite.

The geometrical and mineralogical features of the COx map are given in Table 1. The surface fractions of the clay matrix, calcite and quartz are 50.4%, 25.0% and 13.8%, respectively. Note that the largest side (1563 pixels, 3072 µm) and the smallest side (250 pixels, 500 µm) are perpendicular and parallel to the bedding, respectively.

The second mineral map, hereafter called the Toar map, has been extracted from a large mosaic acquired from a nonimpregnated and dried Tournemire clay rock sample (Fauchille et

al., 2014; Fauchille, 2015). The Tournemire clay rock sample studied has been sampled in the horizontal and cylindrical borehole FD90 in the 1996 East gallery of the Tournemire Underground Research Laboratory (URL) of the French Institute for Radioprotection and Nuclear Safety (IRSN). The sample was located at a depth between 4.20 to 4.40 meters far from the gallery wall, outside the so-called Excavation Damaged Zone. The Tournemire URL is located in a Mesozoic basin on the southern border of the Massif Central (Aveyron, France), in the subhorizontal consolidated argillaceous Toarcian formation (200 meters thick) and marly layers of the Domerian age (50 meters thick). The sample comes from the upper Toarcian formation, whose mineralogical composition shows that clay minerals represent nearly 25-70 wt% of the rock with illite (10-40 wt%) and illite/smectite mixed-layer minerals (5-25 wt%), kaolinite (10-35 wt%) and chlorite (1-5 wt%). The Tournemire clay rock also contains 10-40 wt% of carbonates, 10-30 wt% of quartz, 2-7 wt% of sulfides and less than 2 wt% of feldspars (Cabrera et al., 2001). Similarly to COx map, quartz and calcite are the dominant nonclay minerals and will be the only nonclay minerals to be considered.

The mosaic of interest (7.1 x 5.2 mm<sup>2</sup>, 11302 x 8355 pixels) has been built from one hundred and fifty three back-scattered electron images (spatial resolution of 0.625  $\mu\text{m} \cdot \text{pixel}^{-1}$ ) acquired by Scanning Electron Microscopy (SEM, JEOL JSM 56000LV with an acceleration voltage of 15 kV, a probe current of 5 nA, a working distance of 16.3 mm, a magnification of x200, and a dwell time of 128  $\mu\text{s}$  per pixel). On the mosaic of images, the clay-matrix, carbonates, quartz, sulfides and macropores were differentiated by the MicroPhaseMap© software developed at the IC2MP laboratory in Poitiers, allowing the boundary between the clay matrix and nonclay grains to be determined (Prêt et al., 2010a,b). The mineral map used in this study concerns an extraction (4000x4000pixels) of the most homogeneous part of the mosaic in order to respect at best the statistical homogeneity assumed in all the further  $L_{REA}$  calculations. The geometrical and mineralogical features of this map are also given in Table 1.

Extractions of both maps are given in Figures 2 and 3. Note that both maps were prepared from a polished thin section in a plane perpendicular to the stratigraphic plane. The x-direction indicated in Figures 2 and 3 is parallel to the bedding planes, whereas the z-direction is perpendicular to the bedding.

The results of these image analyses are given in numerical files in which the location and mineral code of each pixel of the mineral maps are indicated. These numerical files are the input files for the  $L_{REA}$  estimate calculations that are presented in the next section.

### **3. Methodologies used to infer the REA size**

#### *3.1 Counting box method*

The counting box method, which is likely the most popular to infer  $L_{REA}$ , starts from a given subdomain or box in the digitalized image. Then, the mean of a surface property (surface mineral contents, surface porosity, physical property, etc.) is calculated within increasing subdomains, often called boxes, until the actual image size is reached (Houben et al., 2014; Klaver et al., 2015). The characteristic size  $L_{REA}$  is considered to be reached when the mean of the considered property does not evolve significantly with the increasing size of boxes. This procedure can be repeated for several starting subdomains to make sure that the inferred  $L_{REA}$  is statistically representative of the whole image. This first method will be named hereafter the classical counting box (CB) method.

Regarding the use of square domains in the CB method, the COx and the Toar maps have been divided into six and four nonoverlapping square areas, respectively, following the partitioning given in Figure 4. These nonoverlapping areas, named  $A_i$  ( $i=1,...,6$  for COx map;  $i=1,...,4$  for Toar map), are associated with the starting of the subdomains, which are defined and discriminated by the coordinates of their center  $C_i$  ( $i=1,...,6$  for COx map;  $i=1,...,4$  for Toar map) (Figure 4). Note that the origin, i.e.,  $x=0$ ,  $z=0$  of the system of coordinates is located in the top left corner of both maps (Figures 2, 3 and 4).

The particular partitioning displayed in Figure 4 is due to two reasons. First, the shape of the CO<sub>x</sub> map is elongated following the z-axis and the center of the initial box could not be located only at the center of this map to investigate the whole map. Second, it was interesting from a statistical viewpoint to compare the  $L_{REA}$  estimates calculated at different areas with a comparable surface and, thus, to check the statistical homogeneity of each map. Note that the number of pixels of each area is sufficient to apply the deterministic CB approach.

### 3.2 “Statistical” Elementary Representative Area (REA)

Kanit et al. (2003; 2006) and Jeulin et al. (2004) extended the classic definition of REV by explicitly integrating the concept of “desired precision” into the calculated effective property. Following their approach, the effective physical properties of heterogeneous materials can be determined not only by one single numerical simulation on a large volume (greater than the REV) of the microstructure but also as the mean value of apparent properties calculated on volumes smaller than the REV, provided that a sufficient number of realizations of the microstructure are considered (e.g., Rolland du Roscoat et al., 2007). Therefore, the “statistical” REV introduced in this manner is not unique; it is defined as a function of the physical properties of each component, the microstructure, the desired precision and the number of realizations. This methodology was used to determine the “statistical” REVs of mechanical and thermal properties of specific random microstructures (Kanit et al., 2003; Pelissou et al., 2009) and of real microstructures of clay rock (Houben et al., 2014; Keller, 2015; 2016a,b). In our study, we will focus on elastic moduli of shale considered as a transverse isotropic rock.

The determination of “statistical” REVs is obtained following a two-step procedure. In the first step, the paramount concept of this approach, the integral range  $A_3$  (or  $A_2$  by considering a 2D image) has to be evaluated.

#### 3.2.1 Determination of integral range

Considering a 2D microstructure, the integral range  $A_2$ , which depends on the studied property, is directly related to the scatter (the dispersion) in apparent properties calculated from several realizations  $n$  of the microstructure of fixed size  $S$ . The integral range gives information on the area size of the microstructure, for which the property measured in this area has a convenient statistical representativity (e.g., Matheron, 1971; Lantuéjoul, 1991).

For an ergodic, stationary random function  $Z(x)$ , and for a large specimen ( $S \gg A_2$ ), the integral range  $A_2$  can be obtained by the following expression (appendix; see also Lantuéjoul, 1991; Kanit et al. 2003; 2006 and Jeulin et al., 2004) as follows:

$$D_Z^2(S) = D_Z^2 \frac{A_2}{S} \quad (1)$$

where  $D_Z^2(S)$  is the variance of the mean value  $\bar{Z}$  over the surface  $S$  and  $D_Z^2$  is the point variance of  $Z(x)$ . Equation (1) is valid for additive properties (e.g., surface fraction or mass density) and, thus, can be rewritten as follows when the surface clay fraction, namely,  $\varphi$  is considered:

$$D_\varphi^2(S) = \bar{\varphi}(1 - \bar{\varphi}) \frac{A_2}{S} \quad (2)$$

where the variance  $D_Z^2$  is  $\bar{\varphi}(1 - \bar{\varphi})$ . As the composition of a physical property  $Z(x)$  (e.g., elastic moduli in our case) in the change of scale is not additive, the latter relation (2) is no more valid, and Kanit et al. (2003) proposed the following modified version:

$$D_Z^2(S) = D_Z^2 \left( \frac{A_2}{S} \right)^\alpha \quad (3)$$

where  $\alpha$  is an exponent that has to be determined. In the case of a two-phase material with the physical property  $Z_1$  for phase 1 and  $Z_2$  for phase 2, the point variance of the random variable  $Z$  is as follows (Kanit et al. 2003; and Jeulin et al., 2004):

$$D_Z^2 = P(1 - P) (Z_1 - Z_2)^2 \quad (4)$$

where  $P$  is the volume fraction of phase 1 or phase 2. In practice, phase 1 and phase 2 are the clay matrix and nonclay inclusions, respectively. In this study, this means that properties

$Z_1$  and  $Z_2$  are the elastic modulus, either the bulk modulus or shear modulus, of the nonclay inclusions and clay matrix, respectively.

As illustrated further, in both cases, i.e., considering the clay fraction  $\varphi$  (equation 2) and a chosen physical property  $Z$  (equation 3), the integral range  $A_2$  is obtained by fitting from the graph of the function  $D_\varphi^2(S)$  or  $D_Z^2(S)$ . In our case, let us recall that  $Z$  is an elastic modulus, either the bulk modulus or shear modulus, the variance  $D_Z^2(S)$  of which is calculated on the partitions of the mineral map in subdomains of a given area  $S$ . The value of  $Z$  for a given subdomain of area  $S$  is obtained from the micromechanical approaches presented in the following section 3.2.2.

### 3.2.1 Determination of the REA size

In a second step, the determination of the integral range allows the calculation of the precision desired to estimate the size  $L_{REA}$ . In the theory of samples, the absolute error  $\varepsilon_{abs}$  and the relative error  $\varepsilon_{rel}$  of the mean effective value  $\bar{Z}$  obtained with  $n$  independent realizations of area  $S$  are deduced from the interval of confidence as follows (e.g., Jeulin et al., 2004):

$$\varepsilon_{abs} = \frac{2 D_Z(S)}{\sqrt{n}} \quad (5)$$

$$\varepsilon_{rel} = \frac{\varepsilon_{abs}}{\bar{Z}} = \frac{2 D_Z(S)}{\bar{Z} \sqrt{n}} \quad (6)$$

Thus, the REA area,  $S_{REA}$ , can now be defined as the area for which  $n$  realization ( $n=1$  for instance) is required to estimate the mean effective property  $\bar{Z}$  with a given relative error ( $\varepsilon_{rel}=5\%$  for instance) provided that the function  $D_Z(S)$  is known.

For instance, if  $Z$  is the surface clay fraction named  $\varphi$ , the parameter  $S_{REA}$ , estimated with a given relative error  $\varepsilon_{rel}$  and a given number of realization  $n$ , can be obtained by combining equations (6) and (2), as follows, provided that the mean effective property  $\bar{\varphi}$  is known:

$$S_{REA} = L_{REA}^2 = \frac{4(1 - \bar{\varphi})A_2}{n \varepsilon_{rel}^2 \bar{\varphi}} \quad (7)$$

In the same way, if  $Z$  is now a physical property, the corresponding parameter  $S_{REA}$ , estimated with a given relative error  $\varepsilon_{rel}$  and a given number of realization  $n$ , can be deduced by combining equations (3), (4), (5) and (6), as follows, provided that the mean effective property  $\bar{Z}$  is known:

$$S_{REA} = L_{REA}^2 = \left[ \frac{4P(1-P)(Z_1 - Z_2)^2}{n \varepsilon_{rel}^2 \bar{Z}^2} \right]^{1/\alpha} A_2 \quad (8)$$

At this stage, two remarks have to be formulated. First, the integral range  $A_2$  in both equations (7) and (8) are not *a priori* similar. The integral range  $A_2$  depends on the property under study, i.e.,  $\varphi$  or  $Z$ , and has to be evaluated separately. Second, this approach assumes that the mean effective properties  $\bar{\varphi}$  and  $\bar{Z}$  are known *a priori*. In practice, the latter are calculated on macroscopic areas supposed to be much greater than the area of the REA.

In summary, a “statistical” REV is therefore determined with the following algorithm (Kanit et al., 2003):

- i) Consider different realizations of the microstructure, i.e., different partitions of the mineral map in subdomains of a given area  $S$ .
- ii) Calculate the mean and the variance of the property of interest of the whole set of partitions under consideration; the graph of the function  $D_{\varphi}^2(S)$  or  $D_Z^2(S)$  is thus obtained.
- iii) Estimate the integral range  $A_2$  from the previous graph, equation (2) or equation (3) (in the later, the exponent  $\alpha$  has to be evaluated as well).
- iv) Define the precision  $\varepsilon_{rel}$  and the number of realization  $n$  to estimate the effective property of interest and calculate the  $L_{REA}$  with equation (7) or equation (8). The value of the effective property,  $\bar{\varphi}$  or  $\bar{Z}$  in equation (7) or equation (8), is independently estimated.

### 3.3.2 Calculations of apparent elastic properties

As mentioned previously, the calculation of the integral range  $A_2$  associated with a given mechanical property requires the values of the average and the variance of the mechanical property calculated over a set of subdomains of the map of interest (step ii). This means that the mechanical property under study has to be calculated in each subdomain of size  $S$  of the map partition. The apparent mechanical property associated with a given subdomain has been estimated in this work by two micromechanical approaches.

#### Anisotropic model

Following the first micromechanical approach, hereafter called the anisotropic model, the transverse isotropic nature of shale is implicitly taken into account. This anisotropic model is itself achieved in two steps. In a first step, the apparent anisotropic stiffness tensor in the subdomain of interest is calculated by an inclusion-based model, i.e., a nonclay spherical grain embedded in a clay transverse isotropic matrix following a differential effective medium (DEM) scheme (e.g., Cosenza et al., 2015b). The latter scheme is widely and successfully used in rock physics to model the elastic wave velocities of numerous rocks (e.g., Hornby et al., 1994; Markov et al., 2005).

The DEM scheme consists of iteratively adding spherical inclusions with diluted concentration into the current effective medium determined in the previous step. At the initial stage, a material with elastic moduli  $\mathbf{C}_M$  is considered as the initial host material. A dilute concentration of spherical inclusions is then added into this initial host; the effective tensor of this new composite can be calculated without considering the interactions between the inclusions. The construction process continues as follows: (a) at each stage, the embedded spherical inclusions are scattered in diluted concentration and (b) the required volume fraction of inclusions is satisfied. At a given step, indexed  $i$ , the small increment of stiffness due to the addition of a small fraction of inclusions,  $df_i$  is given by the following:



$$d\mathbf{C}_i^{ap} = \frac{df_I}{1-f_I} (\mathbf{C}_I - \mathbf{C}_i^{ap}) : [1 + \mathbf{P}_i : (\mathbf{C}_I - \mathbf{C}_i^{ap})] \quad (9)$$

This increment  $d\mathbf{C}_i^{ap}$  must be added to the apparent tensor  $\mathbf{C}_i^{ap}$  obtained in the previous step. Note that the bold capital letters refer here to fourth-order tensors. In our case, the stiffness tensors  $\mathbf{C}_I$  and  $\mathbf{C}_M$  are the stiffness tensor of the isotropic nonclay sphere and the stiffness tensor of the transverse isotropic clay matrix, respectively. The Hill's tensor  $\mathbf{P}_i$  is a function of  $\mathbf{C}_i^{ap}$  and the Eshelby's tensor, which depends on the chosen inclusion-based model, as follows:

$$\mathbf{P}_i = \mathbf{S}_i : (\mathbf{C}_i^{ap})^{-1} \quad (10)$$

The expressions of components of the Hill's tensor for a spherical inclusion in a transversely isotropic medium have been taken from Withers (1989) and Giraud et al. (2007a,b).

In a second step, the apparent tensor  $\mathbf{C}^{ap}$  obtained by DEM is isotropized following the classical decomposition, as follows:

$$\mathbf{C}^{ap,is} = 3K^{is}\mathbf{J} + 2\mu^{is}\mathbf{K} \quad (11)$$

with

$$K^{is} = \frac{C_J^{ap,is}}{3} = \frac{J::\mathbf{C}^{ap}}{3} ; \mu^{is} = \frac{C_K^{ap,is}}{10} = \frac{K::\mathbf{C}^{ap}}{10} \quad (12)$$

$$\mathbf{C}_J^{ap,is} = \frac{1}{3}\mathbf{C}_{iijj}^{ap,is} ; \mathbf{C}_K^{ap,is} = \mathbf{C}_{ijij}^{ap} - \frac{1}{3}\mathbf{C}_{iijj}^{ap} \quad (\text{summation on repeated indices } i,j) \quad (13)$$

and four-rank tensors  $\mathbf{J}$  and  $\mathbf{K}$  obey the following algebraic properties:

$$\mathbf{J} : \mathbf{J} = \mathbf{J} ; \mathbf{K} : \mathbf{K} = \mathbf{K} ; \mathbf{K} : \mathbf{J} = \mathbf{J} : \mathbf{K} = 0 \quad (14)$$

With

$$J_{ijkl} = \frac{1}{3}\delta_{ij}\delta_{kl} ; I_{ijkl} = \frac{1}{2}(\delta_{ik}\delta_{jl} + \delta_{il}\delta_{jk}) ; K_{ijkl} = I_{ijkl} - J_{ijkl} \quad (15)$$

This “isotropization” process of apparent stiffness tensor  $\mathbf{C}^{ap}$  is due to two reasons. The first reason is theoretical. The original methodology described in Kanit et al. (2003; 2006) and Jeulin et al. (2004) involves the isotropic physical properties in equations (3), (4) and (8). We do not know to what extent this methodology can be generalized to anisotropic media, i.e., to

mixtures of anisotropic constituents. In other words, this generalization to anisotropic media has to be proven and its demonstration is beyond the scope of this work. Moreover, it should be noted that despite this “isotropization” process, the calculation of the apparent stiffness tensor of shale is impacted by that of the anisotropic stiffness tensor of the clay matrix and, thus, implicitly depends on the anisotropic nature of rock. The second reason is methodological. This “isotropization” allows the following results to be directly compared to those obtained by a pure isotropic model presented further, since both models provide apparent moduli with the same physical meaning.

Equations (11) to (15) allow the extraction of the apparent isotropized bulk modulus,  $K^{is}$  and the apparent isotropized shear modulus  $\mu^{is}$ , which are used to infer the statistical mechanical REA sizes (i.e., using equation (8)). However, the calculations of  $K^{is}$  and  $\mu^{is}$  and, thus, the  $\mathbf{C}^{ap}$  components require input data, which are the components of the stiffness tensors  $\mathbf{C}_I$  and  $\mathbf{C}_M$ .

The components of stiffness tensor  $\mathbf{C}_I$  correspond to the elastic moduli of nonclay grains (quartz and calcite) whose values have been taken from Mavko et al. (2009). In our calculations, the isotropic elastic moduli of the nonclay phase, i.e., the bulk and shear modulus, are the weighted averages of those of quartz and calcite, where the weights are the gravimetric contents of each phase, as indicated in Table 2. In fact, the pure calcite and quartz phases are anisotropic minerals (e.g., Mavko et al., 2009); their isotropized equivalent elastic properties considered here correspond to random distributions in the orientation and the space of calcite and quartz inclusions (e.g., Ulm et al., 2005; Giraud et al., 2007b).

The elastic moduli of the clay matrix are more difficult to estimate, because the clay phase is also a heterogeneous composite composed of aggregates of clay layers, pores filled with interstitial fluids and, likely, fine nonclay minerals (Figure 1). Consequently, in practice, the elasticity of the clay phase is complex, which makes it difficult to quantitatively characterize

in an experimental viewpoint, and, thus, is poorly constrained in our context. To our knowledge, the most relevant range of transverse-isotropic elastic properties of a clay matrix at the mesoscopic scale has been obtained by Ulm et al. (2005), who used an experimental micromechanics approach by combining nanoindentation measurements with the microporoelasticity theory. These authors have proposed quantitative estimations of elastic moduli, which resulted from the inversion of nanoindentation measurements obtained on three different shale materials at spatial scales of  $10^{-7}$  to  $10^{-5}$  m, which correspond to that of our mineral maps (Ulm et al., 2005; Cosenza et al., 2015b). In our calculations, only the lower bound of the range proposed by Ulm et al., (2005) has been considered (Table 2). Indeed, the values of transverse isotropic moduli considered in Table 2 provided mean values of apparent elastic moduli that are the closest to the reference macroscopic elastic moduli measured in both shales under study. Higher values of clay elastic moduli would have led to much higher values of apparent moduli that are significantly higher than the experimental elastic moduli measured on both shales.

#### *Isotropic model*

In the second micromechanical approach used in this work, hereafter called the isotropic model, the elastic properties of the clay matrix,  $K_M$  and  $\mu_M$ , were not given *a priori*. They have been inverted following a Monte-Carlo procedure to overcome the paramount difficulty of quantitatively characterizing the clay phase elasticity. This inversion procedure has considered the following as input data: the weighted averages of quartz and calcite, the elastic properties of both shales and the reference macroscopic elastic properties, which are all given in Table 2. It was based on a simple micromechanical model, i.e., an inclusion-based model consisting of an isotropic sphere embedded in an isotropic matrix. This isotropic inclusion-based model corresponded again to a DEM approach, which is expressed by the following coupled differential equations (e.g., Christensen, 2012):

$$dK^{ap} = \frac{df_I}{1-f_I} \frac{K_I - K^{ap}}{1 + \frac{K_I - K^{ap}}{K^{ap} + 4/3\mu^{ap}}} \quad (16)$$

$$d\mu^{ap} = \frac{df_I}{1-f_I} \frac{15(1-\nu^{ap})(\mu^{ap} - \mu_I)}{7 - 5\nu^{ap} + 2(4 - 5\nu^{ap}) \frac{\mu_I}{\mu^{ap}}} \quad (17)$$

with

$$\nu^{ap} = \frac{3K^{ap} - 2\mu^{ap}}{2(3K^{ap} + \mu^{ap})} \quad (18)$$

The Monte-Carlo procedure consisted of 10000 random trials of clay matrix moduli ranging between 0 GPa and the reference macroscopic values given in the first column in Table 2. The maximum relative difference between the reference macroscopic value and the calculated macroscopic value by our inverse procedure was less than 2% (Table 3). This difference was considered acceptable with regard to the high uncertainty associated with the quantification of clay matrix elastic moduli.

## 4. Results and Discussion

### 4.1 Counting box REA sizes versus Statistical morphological REA sizes

#### REA sizes inferred by the counting box method

Figures 5 and 6 display the evolutions of the clay fraction calculated on increasing box sizes  $L$  considering the different starting domains of the COx map and Toar map, respectively. Both figures confirm that the calculated clay fraction is a decreasing function of  $L$  and converges to a value, hereafter referred to as the parameter  $\varphi_\infty$ , which is very close to the mean clay fraction obtained on the whole map (Table 1).

Considering the COx map (Figure 5a.), the six curves associated with six starting domains converge to  $\varphi_\infty$  values in the range [48.6-52.4%], including the mean clay fraction  $\overline{\varphi}_{COx}$  of 50.4% calculated on the whole map (Table 1). The difference between these asymptotic values,  $\varphi_\infty$ , and the mean clay fraction  $\overline{\varphi}_{COx}$  is less than 4%. In the same way, in Figure 5b, the

four curves associated with the Toar map converge to  $\varphi_{\infty}$  values in the range [68.5-71.4%], which also include the mean clay fraction  $\overline{\varphi}_{Toar}$  of 69.9% calculated for the whole map (Table 1). The difference between the  $\varphi_{\infty}$  values and  $\overline{\varphi}_{Toar}$  is less than 2.5%.

Below 100 $\mu$ m and 200 $\mu$ m for COx and Toar maps respectively, the curves obtained for the different subdomains presents non correlated and high frequency evolutions. Such a behavior is associated to the occurrence of a few grains with such a large size (Robinet, 2008; Fauchille, 2015) and that large enough box size including several grains should be used to estimate a meaningful REA (Gaboreau et al 2016). For larger box size than 100 $\mu$ m and 200 $\mu$ m for COx and Toar maps respectively, the gap between the curves decreases progressively with low frequency variations. Meaningful REA corresponding to mesoscopic scale (level 3 in Figure 1) could be estimated with an improved accuracy when the box size increases. The careful observation of both maps reveals that grain size is larger for Toar than for COx (compare calcite grains in Figure 2 and carbonates grains in Figure 3), somehow explaining why a larger box size is needed for Toar map to reach a REA as illustrated below (Figures 5a and 5b).

The REA size, i.e.,  $L_{REA}$ , of both maps has been estimated in two steps (Table 4). In the first step, the REA sizes have been calculated for each of the nonoverlapping areas of both maps (6 areas for the COx map and 4 areas for the Toar map) and for two errors or threshold values, i.e.,  $\varepsilon = 0.1$  (10%) and  $\varepsilon = 0.05$  (5%). For each area, the  $L_{REA}$  parameter has been identified as the lowest box size  $L$  for which the calculated mean clay fraction was significantly similar to that of the whole map ( $\overline{\varphi}_{COx}$  or  $\overline{\varphi}_{Toar}$ ), with a maximum error of  $\varepsilon$ . In a second step, the average overall  $L_{REA}$  estimates of all nonoverlapping areas have been calculated for each map. The calculated mean  $L_{REA}$  for a given map has been considered as the  $L_{REA}$  of the latter.

Our results given in Table 4 indicate that the  $L_{REA}$  values are dispersed and decreasing functions of the chosen error or threshold values  $\varepsilon$ . Indeed, in the first case ( $\varepsilon=0.1$ ), the mean values of the  $L_{REA}$  estimates of the COx map and Toar map are 173  $\mu$ m and 129  $\mu$ m, respectively

(Table 2). Whereas in the second case ( $\varepsilon=0.05$ ), the mean values of the  $L_{REA}$  estimates of the COx map and Toar map are much higher, i.e., 234  $\mu\text{m}$  and 441  $\mu\text{m}$ , respectively.

This scatter in the  $L_{REA}$  estimates can also be evidenced by a calculation of the standard deviation of the  $L_{REA}$  estimates associated with nonoverlapping areas (Table 4). Considering the COx map, the standard deviation values of the  $L_{REA}$  estimates increase from 108  $\mu\text{m}$  ( $\varepsilon=0.1$ ) up to 143  $\mu\text{m}$  ( $\varepsilon=0.05$ ). The standard deviation values of the  $L_{REA}$  estimates of the Toar map increase from 72  $\mu\text{m}$  ( $\varepsilon=0.1$ ) up to 267  $\mu\text{m}$  ( $\varepsilon=0.05$ ) (Table 4).

This scatter questions the statistical homogeneity of both maps and could be explained by a small but significant evolution of the microstructure in the x direction and/or in the z direction (i.e., with depth); this is shown in (a), where the  $\varphi_{\infty}$  estimates of the COx map, globally increase with depth, and by (b), where the  $\varphi_{\infty}$  estimates of the Toar map, decrease in the x direction (Table 4).

However, the order of magnitude of all these estimates is comparable to the results from other shales obtained also by the CB method (Opalinus clay: 180-250  $\mu\text{m}$ , Houben et al., 2014; Posidonia shale and Whitby shale: 200  $\mu\text{m}$ , Houben et al., 2016; Bowland shale: 380  $\mu\text{m}$ , Ma et al., 2016; Bakken shale: 176  $\mu\text{m}$ , Liu and Ostadhassan, 2017).

#### *Statistical morphological REA sizes*

Figure 6 displays the mean values of the surface clay fraction  $\bar{\varphi}$  and their corresponding standard deviation values, all calculated on sets of map partitions in subdomains of size  $L$  ranging from 6 to 140  $\mu\text{m}$  (COx map) and from 6.25 to 250  $\mu\text{m}$  (Toar map). Note that these sets of map partitions do not correspond to the partitions  $A_i$  indicated in Figure 4, which have only been used for the CB method. All estimates of the statistical REA sizes in the following have been obtained by considering the whole maps.

Figure 6 suggests the following two comments. First, whatever the subdomain size, the mean values of the surface clay fraction (50.5% for COx map and 69.9% for Toar map) are very close to that of the whole map ( $\bar{\varphi}_{COx}$  or  $\bar{\varphi}_{Toar}$ ). For large subdomain sizes, these mean values are almost equal to  $\bar{\varphi}_{COx}$  or  $\bar{\varphi}_{Toar}$ . Second, the dispersion of the results characterized by their standard deviation decreases with increasing the subdomain size and tends to a plateau for  $L$  values approximately equal to 100  $\mu\text{m}$  and 140  $\mu\text{m}$ , considering the COx map and the Toar map, respectively (Figure 6). Both trends are similar to those already observed for other materials, considering other microstructural properties (porosity and specific surface area) (Zhang et al., 2000; Kanit et al., 2003, 2006).

The decrease in dispersion with  $L$  for both maps evidenced in Figure 6 is also illustrated in Figure 7, which displays the evolution of the pseudovariance  $D_{\varphi}^2(S)/(\bar{\varphi}(1 - \bar{\varphi}))$  as a function of the subdomains area  $S$  (i.e.,  $L^2$ ). In Figure 7, a  $1/S$  fit for a large  $S$  by the least-square method is also indicated to obtain values of the integral range  $A_2$  (equation (2)) required to calculate estimates of the REA size,  $L_{REA}$ , for both maps (equation (7)). The results of the fits for both maps and the  $L_{REA}$  estimates considering one realization ( $n=1$ ) and a range of error [5-10%] are given in Table 5. This table shows two results.

First, the  $L_{REA}$  estimates in Table 5 are rather close to those obtained by the CB method with similar values of errors, i.e., between 5 and 10% (Table 4). Indeed, in the case of the COx map, the statistical REA size,  $L_{REA}$ , is in the range of [205-410  $\mu\text{m}$ ], whereas  $L_{REA}$ , estimated by CB method is in the range of [50-438  $\mu\text{m}$ ] (Table 4). In the case of the Toar map, the statistical  $L_{REA}$  estimates are in the range of [345-696  $\mu\text{m}$ ], whereas the  $L_{REA}$  estimates by the CB method are in the range of [68-749  $\mu\text{m}$ ]. However, the comparison between these two types of estimate is no more relevant for smaller errors  $\varepsilon$  since the  $L_{REA}$  estimate inferred by the statistical method drastically increases as a function of  $1/\varepsilon$  (see equation (10)).

Second, whatever the  $\varepsilon$  value, these results demonstrate that the REA size of the Callovo-Oxfordian claystone is lower than that of the Tournemire argillite. The REA size estimates of the COx map are in the range of [205-410  $\mu\text{m}$ ], whereas those of the Toar map are in the range of [345-696  $\mu\text{m}$ ]. This hierarchy has also been observed in Table 4 following the CB method applied with a  $\varepsilon$  value of 5%.

Figure 8 displays the values of the statistical morphological REA size,  $L_{\text{REA}}$ , as a function of error  $\varepsilon$  (%) for one realization ( $n=1$ ) for both mineral maps. The gray area in Figure 8 indicates the  $L_{\text{REA}}$  estimates for errors in the range of [0.1-10%]. Figure 8 shows that the  $L_{\text{REA}}$  estimates of the COx map are always lower than those of the Toar map, regardless of the  $\varepsilon$  values.

#### 4.2 Statistical morphological REA sizes versus Statistical mechanical REA sizes

Figures 9a and 9b display the evolution of the mean values of the mechanical moduli (bulk modulus and shear modulus) considering both the anisotropic and isotropic models as a function of the size  $L$  of subdomains  $S$ . These figures confirm two trends previously observed in Figure 6. First, the mean values  $\bar{K}$  and  $\bar{G}$  tend rapidly towards plateaus which are close to the reference values for large  $S$ . These asymptotic values depend on the micromechanical model, i.e., the anisotropic or isotropic model used to calculate the mean values  $\bar{K}$  and  $\bar{G}$ . Second, the dispersion of the results decreases again with an increasing subdomain size. In addition, Figures 9a and 9b show that whatever the micromechanical used, the mean values  $\bar{K}$  and their associated dispersion (through standard deviation values) are always greater than the mean values  $\bar{G}$  and its associated dispersion.

The decrease in dispersion with  $L$  for both maps evidenced in Figures 9a and 9b can also be illustrated in Figures 10a and 10b, which display the evolutions of the variance of elastic moduli as a function of the subdomains area  $S$  (i.e.,  $L^2$ ). Figures 10a and 10b also show that the power fit introduced by equation (3) is a relevant model to quantitatively describe these



dispersion evolutions and, hence, to determine the integral range; the calculated regression coefficient  $R^2$  values are all greater than 0.99. For each map, the parameters of these fits, especially the exponents are very close (COx map: 0.89 to 0.896 for the bulk modulus and 0.983 to 1.026 to the shear modulus; Toar map: 0.83 for the bulk modulus and 0.813 to 0.824 to the shear modulus), which illustrates the fact that the calculated variances are of the same order of magnitude for any micromechanical model and any elastic modulus under study. Moreover, Figure 10b shows that the variances of the elastic moduli of the Toar map are almost independent of the chosen micromechanical model.

Figures 11a and 11b show the mechanical  $L_{REA}$  values inferred from the calculations of integral range values obtained from Figures 10a and 10b and equation (8). These figures highlight at least three results. First, in the case of both mineral maps under study, these figures show that for any micromechanical model and any elastic modulus under consideration, the mechanical  $L_{REA}$  is significantly greater than morphological  $L_{REA}$  (compare Figures 11a and 11b to Figure 8). The concept of  $L_{REA}$  fundamentally depends on the property of interest. Second, all things being equal, the mechanical  $L_{REA}$  estimates of the COx map are lower than those of the Toar map (see also Table 6). This hierarchy previously observed for the morphological  $L_{REA}$  estimates (see Figure 8) is retrieved when the mechanical properties are considered. Third, for any mineral map and any micromechanical model, the  $L_{REA}$  estimates of the bulk modulus are lower than those of the shear modulus (Table 6). However, this difference between both estimates is more tenuous in the case of the Toar map for which  $L_{REA}$  estimates for a given  $\varepsilon$  value can be considered as similar and insensitive to the chosen micromechanical models in a first order approach (Table 6).

#### *4.3 Impacts of anisotropy and heterogeneity at the map scale*

The calculations of different  $L_{REA}$  in this study are based on equations (7) and (8), which *a priori* assume an isotropy of mechanical properties of interest. In this framework, the well-

known anisotropic nature of shale raises a difficulty that has been bypassed here by “isotropizing” the transverse isotropic stiffness tensor of the clay matrix. Moreover, to study the impact of this underlying anisotropy introduced in this manner, a pure isotropic micromechanical model has been introduced for comparison purposes. Thus, the main objective associated with the introduction of an implicit anisotropic model and a pure isotropic model was to address the following question: what is the impact of the underlying mechanical anisotropy of shale on its  $L_{REA}$  estimates?

All the outcomes provided by this work show that the following qualitative results do not depend finally on the chosen micromechanical models and, thus, would be independent of the underlying anisotropic nature of shale. These outcomes are as follows: (i) The mechanical  $L_{REA}$  estimates are greater than the morphological ones; (ii) The mechanical  $L_{REA}$  estimates of the Toar map are greater than those of the COx map; and (iii) The mechanical  $L_{REA}$  estimates of the apparent shear modulus are greater than those of the bulk modulus.

The second underlying assumption used in this work is the statistical homogeneity of both mineral maps, meaning, from a statistical viewpoint, that the stationarity assumption of the properties of interest is satisfied on both maps (see appendix and Lantuéjoul, 1991; Torquato, 2013). Let us recall that the stationary assumption means here that the statistical properties implied in our calculations are invariant by translation, i.e., they do not depend on the absolute position in the mineral maps. In our case, the  $L_{REA}$  estimated by the CB method strongly depends on the starting domain chosen in the mineral maps, as shown by the high values of standard deviation of the calculated mean  $L_{REA}$  values (Table 4). This strong spatial variability of the  $L_{REA}$  estimate is a serious indication that the stationarity assumption would not be fulfilled. This indication seems to be confirmed at least for the Toar map by the statistical approach promoted in this study. Figure 12 clearly shows that the 1/S fit associated with equation (2) is finally in poor agreement with the calculated pseudovariance of the clay fraction

used to calculate the integral range  $A_2$  (coefficient of determination  $R^2$  equal to 0.36). According to Lantuéjoul (1991), a poor agreement between equation (2) and the measurements would indicate that the image under study would not satisfy the stationary assumption. This result suggests that a combined use of the simple CB method and a calculation of the integral range following the statistical approach applied here would be a simple and efficient way to check *a posteriori* the statistical homogeneity of the maps and images under study at the mesoscopic scale, which is scarcely ensured in practice. This suggestion and these results have to be obviously verified on other mineral maps.

## 5. Concluding remarks

The main objective of this work was to provide new estimates of REA sizes of the following two shales actively studied in the framework of the deep disposal of radioactive waste: Callovo-Oxfordian (COx) claystone from the Meuse/Haute-Marne underground research laboratory (Eastern France) and Toarcian argillite from the experimental station of Tournemire (Southern France). The  $L_{REA}$  estimates obtained from two mineral maps at a mesoscopic scale have been calculated by the classic counting box (CB) method and a statistical approach that introduces the concept of a “statistical” REA. Following this approach, a “statistical” REA is related not only to the microstructure and the properties of each of the components but, above all, to a given precision in the estimation of the effective property depending on the number of realizations “that one is ready to generate” (Jeulin et al., 2004). The probabilistic concept of realization here is any representation or observation of the microstructure considered with a given size and a given fraction of heterogeneities, i.e., in our case, from a practical viewpoint, a subdomain of a given area of a mineral map. This statistical approach requires the calculations of the apparent elastic moduli in this subdomain or in the set of subdomains, which have been achieved here by using two micromechanical models. The first micromechanical model consisted of an anisotropic inclusion-based model for which

spherical nonclay grain is embedded in a clay matrix, in which the values of its transverse isotropic stiffness tensor have been taken from literature. The second micromechanical model was an isotropic inclusion-based model for which spherical nonclay grain is embedded in a clay matrix; the elastic moduli values have been inverted by a Monte-Carlo approach from the macroscopic engineering moduli measured on both shales under study. The calculations performed following this statistical approach have shown the following results:

- The morphological  $L_{REA}$  estimates inferred for the statistical approach are of the same order of magnitude as those found in the literature and obtained by the classic CB method by considering the values of the relative errors, i.e., between 5 and 10%.
- For any micromechanical model and any elastic modulus under consideration, the mechanical  $L_{REA}$  is significantly greater than morphological  $L_{REA}$ . Our study confirms that the concept of  $L_{REA}$  fundamentally depends on the property of interest.
- The mechanical  $L_{REA}$  estimates of the Toar map are greater than those of the COx map. This is also the case for the morphological  $L_{REA}$  estimates inferred for a low relative error of 5%.
- All things being equal, the mechanical  $L_{REA}$  estimates of shear modulus are greater than those of the bulk modulus

Moreover, our study highlights two additional aspects. First, all the outcomes provided by this work show that these previous qualitative results do not depend on the chosen micromechanical models and, thus, would be ultimately independent of the underlying anisotropic nature of the shale. Second, a combined use of the simple CB method with a calculation of the integral range following this statistical approach strongly brings into question the statistical homogeneity of the Toar map. Consequently, this result suggests that this coupled

approach would be a simple and efficient way to check *a posteriori* the statistical homogeneity of the maps and images under study, which is scarcely ensured in practice. The application and validation of such a coupled approach on other mineral maps is obviously one natural perspective of this work.

Finally, this work strongly suggests the need for further investigations in two directions. First, this work has considered the definitions of REA or REV initially established on homogeneous and isotropic media, but one may wonder if these definitions are still valid or can be refined for strongly anisotropic media made of anisotropic components. Second, our approach has highlighted the crucial role of the anisotropic mechanical properties of the clay matrix. The accurate measurements of these mechanical parameters are still a challenging area of experimental research.

## **Appendix. The integral range**

Here, we borrow definitions and notations from Lantuéjoul (1991). Let us consider (i) a domain of area  $S$  that is sufficiently large to ensure that the properties of interest may be estimated with good precision (note that the following concepts are defined in 2D but their generalization in 3D is straightforward), and (ii) a stationary random function  $(Z(x))_{x \in \mathbb{R}^d}$  with mean  $\mu$  and variance  $\sigma^2 = D_Z^2$ , which are both unknown. In the context of randomness, the average value of  $Z$ , named  $\bar{Z}$ , over the area  $S$  can be evaluated by the following estimator:

$$Z(S) = \frac{1}{S} \int_S Z(x) dx \quad (A1)$$

and the variance of this estimator, namely,  $D_Z^2(S)$ , is given by the following:

$$D_Z^2(S) = \frac{1}{S^2} \int_S \int_S C(y - x) dx dy \quad (A2)$$

where  $C(y - x)$  is the autocovariance function of the *stationary* random function  $Z(x)$  expressed by the following:

$$C(y-x) = C(h) = E\{[Z(x) - E(Z)][Z(x+h) - E(Z)]\} \quad (A3)$$

In other words, the statistical property  $D_Z^2(S)$  defined by equation (A2) can be seen as the variance of the average value  $\bar{Z}(S)$ , which is in fact the effective property to be determined. As explained further, this statistical property  $D_Z^2(S)$  is directly linked to the concept of the integral range. The next step requires the definition of the ergodicity assumption, as follows: a random function  $Z$  is ergodic if variance  $D_Z^2(S)$  tends toward 0 when the size of the domain  $S$  becomes infinite, as follows:

$$\lim_{S \rightarrow \infty} D_Z^2(S) = 0 \quad (A4)$$

The concept of the integral range, namely,  $A_2$ , is then introduced to define the rate of decrease of this variance at large distances, i.e., in large areas, as follows:

$$A_2 = \lim_{S \rightarrow \infty} S \frac{D_Z^2(S)}{D_Z^2} \quad (A5)$$

This quantity does not always exist. When it does exist, it is nonnegative. If  $A < +\infty$ , for large  $S$ , then:

$$D_Z^2(S) \approx \frac{D_Z^2 A_2}{S} \quad (A6)$$

Now we return to the problem met in practice. Suppose that the domain  $S$  can be decomposed into a union of disjoint subdomains,  $s_1, \dots, s_k$ , all of the same shape and of the same size  $s$ . In each subdomain  $s_i$ , the average value taken by  $Z(x)$  over  $s_i$  is as follows:

$$Z(s_i) = \frac{1}{s} \int_{s_i} Z(x) dx \quad (A7)$$

where  $s$  denotes the area of  $s_i$ . The “dispersion variance” of the  $Z(s_i)$  is now defined as follows:

$$\sigma^2(s|S) = E \left\{ \frac{1}{k} \sum_{i=1}^k [Z(s_i) - Z(S)]^2 \right\} \quad (A8)$$

or

$$\sigma^2(s|S) = D_Z^2(s) - D_Z^2(S) \quad (A9)$$

Suppose now that the integral range is finite and nonzero and that the area  $s$  is very large compared to  $A_2$ . In this case, the approximation formula (A6) is valid and then equation (A9) can be rewritten as follows:

$$\sigma^2(s|S) \approx D_Z^2 A_2 \left( \frac{1}{s} - \frac{1}{S} \right) \quad (A10)$$

Now if  $S$  has been divided into a large number of subdomains, then  $1/S$  can be considered as negligible compared to  $1/s$  and therefore:

$$\sigma^2(s|S) \approx \frac{D_Z^2 A_2}{s} \quad (A11)$$

Thus, the dispersion variance is inversely proportional to the area of the subdomains,  $s$ . From a practical viewpoint, it is this dispersion variance that is calculated to obtain an estimation of  $A_2$  by a fitting procedure.

**Acknowledgments.** We thank the NEEDS-MIPOR – VARAPE (VARIabilité spatiale des propriétés de l'Argilite au travers d'une approche numérique-expérimentale à Plusieurs Echelles) program for its financial support. A part of this study was also performed in the framework of the research project "ExCiTING" funded by the French National Research Agency (grant agreement ANR-17-CE06-0012). The authors also acknowledge financial support from the European Union (ERDF) and "Région Nouvelle Aquitaine".

## References

- Abou-Chakra Guéry, A., Cormery, F., Shao, J.-F., & Kondo, D. (2010). A comparative micromechanical analysis of the effective properties of a geomaterial: effect of mineralogical compositions. *Computers and Geotechnics*, 37, 585-593.
- Andra (2005). Dossier 2005 Argile: Synthesis. Evaluation of the feasibility of a geological repository in an argillaceous formation. Andra, France (available at [www.andra.fr](http://www.andra.fr)).

715 Aplin, A. C., & Larter S. R. (2005). Fluid flow, pore pressure, wettability and leakage in  
716 mudstone cap rocks, in: Evaluating Fault and Cap Rock Seals, American Association of  
717 Petroleum Geologists Hedberg Series N°2, edited by P. Boulton, and J Kaldi, pp 1-12,  
718 AAPG, Tulsa, USA.

719 Bennett, R.H., O'Brien, N.R. & Hulbert, M.H. (1991). Determinants of clay and shale  
720 microfabric signatures: Processes and mechanisms. In: Bennett, R., Bryant, W., Hulbert,  
721 M. (eds), Microstructure of fine grained sediments: from mud to shale, Springer-Verlag,  
722 New York, Chapter 2, 5-32.

723 Biot, M. A. (1941). General theory of three-dimensional consolidation. *Journal of Applied*  
724 *Physics*, 12(2), 155-164.

725 Bobko, C., & Ulm, F.J. (2008). The nano-mechanical morphology of shale. *Mechanics of*  
726 *Materials*, 40(4), 318-337.

727 Cabrera, J., Beaucaire, C., Bruno, G., De Windt, L., Genty, A., Ramambasoa, N., Rejeb, A.,  
728 Savoye, S., & Volant, P. (2001). *Projet Tournemire : Synthèse des Résultats des*  
729 *Programmes de Recherche 1995/1999*. IRSN Report.

730 Cariou, S., Dormieux, L., & Skoczylas, F. (2013). An original constitutive law for Callovo-  
731 Oxfordian argillite, a two-scale double-porosity material. *Applied. Clay Science*, 80, 18-  
732 30.

733 Christensen, R. M. (2012). *Mechanics of composite materials*. Courier Corporation.

734 Conil, N., Talandier, J., Djizanne, H., de La Vaissière, R., Righini-Waz, C., Auvray, C.,  
735 Morlot ; C., & Armand, G. (2018). How rock samples can be representative of in situ  
736 condition: A case study of Callovo-Oxfordian claystones., *Journal of Rock Mechanics*  
737 *and Geotechnical Engineering*, 10(4), 613-623.

738 Cosenza, P., Prêt, D., Giraud, A., & Hedan, S. (2015a). Effect of the local clay distribution on  
739 the effective elastic properties of shales. *Mechanics of Materials*, 84, 55-74.



740 Cosenza, P., Prêt, D., & Zamora, M. (2015b). Effect of the local clay distribution on the  
741 effective electrical conductivity of clay rocks. *Journal of geophysical research: solid*  
742 *earth*, 120(1), 145-168.

743 Cousin, I., Levitz, P., & Bruand, A. (1996). Three-dimensional analysis of a loamy-clay soil  
744 using pore and solid chord distributions. *European Journal of Soil Science*, 47(4), 439-  
745 452.

746 Fauchille, A. L., Hedan, S., Prêt, D., Valle, V., Cabrera, J., & Cosenza, P. (2014). Relationships  
747 between desiccation cracking behavior and microstructure of the Tournemire clay rock  
748 by coupling DIC and SEM methods. *Proceedings of IS on Geomechanics from Micro*  
749 *to Macro, Cambridge, UK. CRC Press/Balkema, Leiden, The Netherlands*, 1421-1424.

750 Fauchille, A.L., (2015). Déterminismes microstructuraux et minéralogiques de la fissuration  
751 hydrique dans les argilites de Tournemire : apports couplés de la pétrographie  
752 quantitative et de la corrélation d'images numériques, PhD thesis of Poitiers University  
753 (France) (in French).

754 Fauchille, AL van den Eijnden, A.P., Ma L., Chandler, M., Taylor, K.G., Madi, K., Lee, P.D,  
755 Rutter, E. (2018). Variability in spatial distribution of mineral phases in the Lower  
756 Bowland Shale, UK, from the mm- to  $\mu$ m-scale: Quantitative characterization and  
757 Modeling, *Marine and Petroleum Geology*, in press.

758 Gaboreau, S., Robinet, J. C., & Prêt, D. (2016). Optimization of pore-network characterization  
759 of a compacted clay material by TEM and FIB/SEM imaging. *Microporous and*  
760 *Mesoporous Materials*, 224, 116-128.

761 Giraud, A., Huynh, Q. V., Hoxha, D., & Kondo, D. (2007a). Effective poroelastic properties of  
762 transversely isotropic rock-like composites with arbitrarily oriented ellipsoidal  
763 inclusions. *Mechanics of Materials*, 39(11), 1006-1024.

764 Giraud, A., Huynh, Q. V., Hoxha, D., & Kondo, D. (2007b). Application of results on Eshelby  
765 tensor to the determination of effective poroelastic properties of anisotropic rocks-like  
766 composites. *International Journal of Solids and Structures*, 44(11), 3756-3772.

767 Hornby, B. E., Schwartz, L. M., & Hudson, J. A. (1994). Anisotropic effective-medium  
768 modeling of the elastic properties of shales. *Geophysics*, 59(10), 1570-1583.

769 Houben, M. E., Desbois, G., & Urai, J. L. (2014). A comparative study of representative 2D  
770 microstructures in Shaly and Sandy facies of Opalinus Clay (Mont Terri, Switzerland)  
771 inferred from BIB-SEM and MIP methods. *Marine and Petroleum Geology*, 49, 143-  
772 161.

773 Houben, M. E., Barnhoorn, A., Wasch, L., Trabuco-Alexandre, J., Peach, C. J., & Drury, M.  
774 R. (2016). Microstructures of early jurassic (Toarcian) shales of Northern  
775 Europe. *International Journal of Coal Geology*, 165, 76-89.

776 Jeulin, D., Kanit, T., & Forest, S. (2004). Representative volume element: a statistical point of  
777 view. In *Continuum Models and Discrete Systems* (pp. 21-27). Springer, Dordrecht.

778 Jakobsen, M.J., Hudson, A., Johansen, T.A. (2003). T-matrix approach to shale acoustics,  
779 *Geophysical Journal International*, 154, 533-558.

780 Jorand R. 2006, Etude expérimentale de la conductivité thermique: application au forage  
781 EST205 du site de Meuse/Haute Marne (Andra), Ph-D Thesis, University of Denis  
782 Diderot (Paris) (in French).

783 Kameda, A., Dvorkin, J., Keehm, Y., Nur, A., & Bosl, W. (2006). Permeability-porosity  
784 transforms from small sandstone fragments. *Geophysics*, 71(1), N11-N19.

785 Kanit, T., Forest, S., Galliet, I., Mounoury, V., & Jeulin, D. (2003). Determination of the size  
786 of the representative volume element for random composites: statistical and numerical  
787 approach. *International Journal of solids and structures*, 40(13-14), 3647-3679.

788 Kanit, T., N'Guyen, F., Forest, S., Jeulin, D., Reed, M., & Singleton, S. (2006). Apparent and  
789 effective physical properties of heterogeneous materials: representativity of samples of  
790 two materials from food industry. *Computer Methods in Applied Mechanics and*  
791 *Engineering*, 195(33-36), 3960-3982.

792 Khdir, Y. K., Kanit, T., Zaïri, F., & Nait-Abdelaziz, M. (2013). Computational homogenization  
793 of elastic-plastic composites. *International Journal of Solids and Structures*, 50(18),  
794 2829-2835.

795 Keller, L. M., Holzer, L., Schuetz, P., & Gasser, P. (2013). Pore space relevant for gas  
796 permeability in Opalinus clay: Statistical analysis of homogeneity, percolation, and  
797 representative volume element. *Journal of Geophysical Research: Solid Earth*, 118(6),  
798 2799-2812.

799 Keller, L. M. (2015). On the representative elementary volumes of clay rocks at the  
800 mesoscale. *Journal of Geology and Mining Research*, 7(6), 58-64.

801 Keller, L. M. (2016a). Pore geometry effects on elastic properties of Opalinus  
802 Clay. *Geophysics*, 81(5), D543-D551.

803 Keller, L. M. (2016b). Porosity anisotropy of Opalinus Clay: implications for the poroelastic  
804 behaviour. *Geophysical Journal International*, 208(3), 1443-1448.

805 Klaver, J., Desbois, G., Littke, R., & Urai, J. L. (2015). BIB-SEM characterization of pore space  
806 morphology and distribution in postmature to overmature samples from the Haynesville  
807 and Bossier Shales. *Marine and petroleum Geology*, 59, 451-466.

808 Lantuejoul, C. (1991). Ergodicity and integral range. *Journal of Microscopy*, 161(3), 387-403.

809 Levin, V.M., & Markov, M.G. (2005). Elastic properties of inhomogeneous transversely  
810 isotropic rocks. *International Journal of Solids and Structures*, 42(2), 393-408.

811 Liu, K., & Ostadhassan, M. (2017). Quantification of the microstructures of Bakken shale  
812 reservoirs using multi-fractal and lacunarity analysis. *Journal of Natural Gas Science and*  
813 *Engineering*, 39, 62-71.

814 Loucks, R. G., Reed, R. M., Ruppel, S. C., & Hammes, U. (2012). Spectrum of pore types and  
815 networks in mudrocks and a descriptive classification for matrix-related mudrock pores.  
816 *AAPG bulletin*, 96(6), 1071-1098.

817 Ma, L., Fauchille, A. L., Dowey, P. J., Pilz, F. F., Courtois, L., Taylor, K. G., & Lee, P. D.  
818 (2017). Correlative multi-scale imaging of shales: a review and future  
819 perspectives. *Geological Society, London, Special Publications*, 454, SP454-11.

820 Markov, M., Levine, V., Mousatov, A., & Kazatchenko, E. (2005). Elastic properties of double-  
821 porosity rocks using the differential effective medium model. *Geophysical Prospecting*  
822 53(5), 733-754.

823 Matheron, G. (1971). The theory of regionalized variables and it applications. *Ecole des Mines*  
824 *de Paris, Paris*.

825 Mavko, G., Mukerji, T., & Dvorkin, J. (2009). The rock physics handbook: Tools for seismic  
826 analysis of porous media. Cambridge University Press.

827 Niandou, H., Shao, J. F., Henry, J. P., & Fourmaintraux, D. (1997). Laboratory investigation of  
828 the mechanical behaviour of Tournemire shale. *International Journal of Rock Mechanics*  
829 *and Mining Sciences*, 34(1), 3-16.

830 Ortega, J. A., Ulm, F. J., & Abousleiman, Y. (2007). The effect of the nanogranular nature of  
831 shale on their poroelastic behavior. *Acta Geotechnica*, 2(3), 155-182.

832 Ortega, J. A., Ulm, F. J., & Abousleiman, Y. (2009). The nanogranular acoustic signature of  
833 shale. *Geophysics*. 74(3), D65-D84.

834 Pelissou, C., Baccou, J., Monerie, Y., & Perales, F. (2009). Determination of the size of the  
835 representative volume element for random quasi-brittle composites. *International*  
836 *Journal of Solids and Structures*, 46(14-15), 2842-2855.

837 Prêt, D. (2003). Nouvelles méthodes quantitatives de cartographie de la minéralogie et de la  
838 porosité dans les matériaux argileux : application aux bentonites compactées des  
839 barrières ouvragées, p. 257. PhD-Thesis, Poitiers University, France (in French).

840 Prêt, D., Sammartino, S., Beaufort, D., Meunier, A., Fialin, M., Michot, L. (2010a). A new  
841 method for quantitative petrography based on image processing of chemical elements  
842 maps : Part I. Mineral mapping applied to compacted bentonites. *American*  
843 *Mineralogist*, 95, 1379-1388.

844 Prêt, D., Sammartino, S., Beaufort, D., Fialin, M., Sardini, P., Cosenza, P., Meunier, A. (2010b).  
845 A new method for quantitative petrography based on image processing of chemical  
846 elements maps : Part II. Semi-quantitative porosity maps superimposed on mineral  
847 maps. *American Mineralogist*, 95, 1389-1398.

848 Pusch, R., (2006). Clays and nuclear waste management. In: Handbook of Clay Science,  
849 Editors: Bergaya, F., Theng, B.K.G., Lagaly, G., Developments in Clay Science,  
850 Elsevier, 703-716.

851 Robinet, J. C. Minéralogie, porosité et diffusion dans l'argilite du Callovo-Oxfordien de Bure  
852 (Meuse/Haute-Marne, France) de l'échelle centimétrique à micrométrique. PhD thesis,  
853 Poitiers University (France) (in French).

854 Robinet, J.C., Prêt, D., Sardini, P., & Coelho, D. (2007). Solute diffusion in Bure argillite at  
855 millimeter to micrometer scales: the role of mineral and microstructural heterogenities,  
856 3<sup>rd</sup>. Annual Workshop Proceedings 6<sup>th</sup> EC FP – FUNMIG IP, Edinburgh 26<sup>th</sup>-29<sup>th</sup>  
857 November 2007.

858 Robinet, J. C., Sardini, P., Coelho, D., Parneix, J.C., Prêt, D., Sammartino, S., & Altmann, S.  
859 (2012). Effects of mineral distribution at mesoscopic scale on solute diffusion in a clay-  
860 rich rock: Example of the Callovo-Oxfordian mudstone (Bure, France). *Water*  
861 *Resources Research*, 48(5).

862 Rolland du Roscoat, S. R., Decain, M., Thibault, X., Geindreau, C., & Bloch, J. F. (2007).  
863 Estimation of microstructural properties from synchrotron X-ray microtomography and  
864 determination of the REV in paper materials. *Acta Materialia*, 55(8), 2841-2850.

865 Song, Y., Davy, C. A., Troadec, D., Blanchenet, A. M., Skoczylas, F., Talandier, J., & Robinet,  
866 J. C. (2015). Multi-scale pore structure of COx claystone: Towards the prediction of fluid  
867 transport. *Marine and Petroleum Geology*, 65, 63-82.

868 Torquato, S. (2013). Random heterogeneous materials: microstructure and macroscopic  
869 properties (Vol. 16). Springer Science & Business Media.

870 Torquato S., & Stell, G. (1982). Microstructure of two-phase random media. I. The  $n$ -point  
871 probability functions, *Journal of Chemical Physics*, 77, 2071.

872 Ulm, F. J., Delafargue, A., & Constantinides, G. (2005). Experimental microporomechanics. In  
873 *Applied micromechanics of porous materials* (pp. 207-288). Springer Vienna.

874 Withers, P.J. (1989). The determination of the elastic field of an ellipsoidal inclusion in a  
875 transversely isotropic medium, and its relevance to composite materials. *Philosophical*  
876 *Magazine*, A. 59(4), 759-781.

877 Zhang, D., Zhang, R., Chen, S., & Soll, W. E. (2000). Pore scale study of flow in porous media:  
878 Scale dependency, REV, and statistical REV. *Geophysical research letters*, 27(8),  
879 1195-1198.

880 Zhang, W., Zhao, Q., Huang, R., Ma, D., Chen, J., Xu, P., & Que, J. (2017). Determination of  
881 Representative Volume Element Considering the Probability that a Sample Can

882 Represent the Investigated Rock Mass at Baihetan Dam Site, China. *Rock Mechanics*  
883 *and Rock Engineering*, 50(10), 2817-2825.  
884  
885  
886

## Table captions

Table 1. *Geometrical and mineralogical features of both mineral maps used in this work.*

Table 2. Input data for the calculations of apparent elastic properties of both shales under study.

Table 3. Inverted values of isotropic moduli of the clay phase by the Monte Carlo procedure (isotropic model).

Table 4. REA estimates obtained from the counting box method.

Table 5. Morphological REA size estimates by statistical approach (n=1; error ranging between 5 and 10%). The results of inverse regression and integral range are also given.

Table 6. Recapitulation of mechanical REA size estimates by statistical approach (n=1; error ranging between 5 and 10%).

## Figure captions

Figure 1. Microstructure of clay-rocks at various scales (modified from Ulm et al. 2005; Sarout and Guéguen, 2008; Cosenza et al., 2015a).

Figure 2. Extraction of the mineral COx map used in this work (modified from Cosenza et al., 2015a).

Figure 3. Extraction of the mineral Toar map used in this work (modified from Fauchille, 2015).

Figure 4. A. Partitioning of the COx map only used for the counting box method. B. Partitioning of the Toar map used for the counting box method. In both cases, the direction of bedding is indicated.

Figure 5 Estimation of the Representative Elementary Area (REA) size of mineral maps by counting box method. Evolution of mean clay fraction with increasing subdomain size (box) and for different starting domains. The coordinates of starting domains are given in the captions boxes (see the origin of the system of Cartesian coordinates in Figures 2 and 3).

a. COx map. The x-coordinates of the starting domains is 250  $\mu\text{m}$ . The horizontal dashed lines indicate the range of mean clay fraction corresponding to  $(1 \pm \varepsilon)\bar{\phi}_{COx}$  with  $\bar{\phi}_{COx}=0.504$  (50.4%) and  $\varepsilon=0.1$ (10%)

b. Toar map. The horizontal dashed lines indicate the range [62.9-76.9%] corresponding to  $(1 \pm \varepsilon)\bar{\phi}_{Toar}$  with  $\bar{\phi}_{Toar}=0.699$  (69.9%) and  $\varepsilon=0.1$ (10%).

Figure 6. Evolution of the mean clay fraction and related standard deviation *versus* the subdomain size for both maps.



Figure 7. Determination of the “morphological” integral range  $A_2$ . Evolution of the pseudovariance of the clay fraction, i.e., Variance ( $\bar{\varphi}_{arg}(1-\bar{\varphi}_{arg})$ ) as a function of  $1/S$ , where  $S$  is the box size area. A linear fit is indicated by a bold line. a. COx map. b. Toar map.

Figure 8. REA size,  $L_{REA}$  ( $\mu m$ ), as a function of error (%) for one realization ( $n=1$ ) for both mineral maps.

Figure 9. Mean value and dispersion (standard deviation) of the apparent elastic moduli as a function of the subdomain size  $L$  in the case of the anisotropic model and isotropic model. a: COx map. b: Toar map.

Figure 10. Determination of the “mechanical” integral range  $A_2$ . Evolution of the variance of the elastic modulus of the anisotropic and isotropic models as a function of the subdomain area. Power fits are also indicated to calculate the integral range values. a. COx map. b. Toar map.

Figure 11. Mechanical REA size,  $L_{REA}$  ( $\mu m$ ), as a function of error (%) for one realization ( $n=1$ ). Both elastic moduli, i.e., the bulk modulus and shear modulus; both micromechanical models, i.e., the anisotropic model and isotropic model, are considered. a. COx map. b. Toar map.

Figure 12. Zoom of the evolutions of the pseudo-variance of clay fraction i.e., Variance( $\bar{\varphi}_{arg}(1-\bar{\varphi}_{arg})$ ) as a function of subdomain area of both maps.  $R^2$  values of both fits are also given.

940

941 Table 1. *Geometrical and mineralogical features of both mineral maps used in this work.*

Map	Resolution ( $\mu\text{m}$ )	Total number of pixels	Dimensions (pixels)	Dimensions ( $\mu\text{m}$ )	Clay minerals (%)	Quartz (%)	Calcite (%)
COx	2	384 000	250 x 1536	500 x 3072	50.4	13.8	25.0
Toar	0.625	$16 \cdot 10^6$	4000 x 4000	2500 x 2500	69.9	13.2	14.1

942

943

944

Table 2. Input data for the calculations of apparent elastic properties of both shales under study.

Shale	Macroscopic (reference) shale elastic modulus (GPa)	Non-clay phase Isotropic elastic modulus Weighted average (GPa) <sup>b</sup>	Clay phase Transverse isotropic (undrained) modulus (GPa) <sup>c</sup>
	Bulk modulus <sup>a</sup>	Bulk modulus	C <sub>11</sub> = 14.3
Callovo-Oxfordian claystone	11.5	56.3	C <sub>12</sub> =4.6
	Shear modulus <sup>a</sup>	Shear modulus	C <sub>13</sub> =2.7
	5.3	38.5	C <sub>33</sub> =8.9
			C <sub>44</sub> =2.8
	Bulk modulus <sup>d</sup>	Bulk modulus	C <sub>11</sub> = 14.3
Tournemire argillite	9.2	53.9	C <sub>12</sub> =4.6
	Shear modulus <sup>d</sup>	Shear modulus	C <sub>13</sub> =2.7
	6.5	37.5	C <sub>33</sub> =8.9
			C <sub>44</sub> =2.8

<sup>a</sup>ANDRA (2009) (undrained Poisson ratio:  $\nu^u=0.3$ )

<sup>b</sup>Table 1 and Mavko et al. (2009)

<sup>c</sup>Ulm et al. (2005); Cosenza et al. (2015b)

<sup>d</sup>Niandou et al. (1997)

Table 3. Inverted values of isotropic moduli of clay phase by Monte Carle procedure (isotropic model).

Shale	Clay phase Inverted isotropic modulus (GPa)	Relative difference between reference value and calculated value from inverted clay phase moduli (%)
Callovo-Oxfordian claystone	Bulk modulus 5.0	Bulk modulus 0.3
	Shear modulus 1.6	Shear modulus 1.4
Tournemire argillite	Bulk modulus 5.3	Bulk modulus 1.6
	Shear modulus 3.7	Shear modulus 0.1

955 Table 4. REA estimates obtained by counting box method.

956

Map	Area ( $A_i$ )	Center of area ( $C_i$ )	Asymptotic value ( $\varphi_\infty$ ) (%)	REA estimate ( $L_{REA}$ ) ( $\mu\text{m}$ ) $\varepsilon=0.1$ (10%)	REA estimate ( $L_{REA}$ ) ( $\mu\text{m}$ ) $\varepsilon=0.05$ (5%)
COx	A1	C1 (x=250 $\mu\text{m}$ , z=250 $\mu\text{m}$ )	49.0	262	314
	A2	C2 (x=250 $\mu\text{m}$ , z=750 $\mu\text{m}$ )	48.6	322	438
	A3	C3 (x=250 $\mu\text{m}$ , z=1250 $\mu\text{m}$ )	49.4	128	170
	A4	C4 (x=250 $\mu\text{m}$ , z=1750 $\mu\text{m}$ )	51.6	72	86
	A5	C5 (x=250 $\mu\text{m}$ , z=2250 $\mu\text{m}$ )	52.4	202	310
	A6	C6 (x=250 $\mu\text{m}$ , z=2500 $\mu\text{m}$ )	51.5	50	86
			Mean: 51.5	Mean: 172.7	Mean: 234.0
			St. Dev.: 1.6	St. Dev.: 108.0	St. Dev.: 142.6
Toar	A1	C1 (x=625 $\mu\text{m}$ , z=625 $\mu\text{m}$ )	71.4	163	179
	A2	C2 (x=1250 $\mu\text{m}$ , z=625 $\mu\text{m}$ )	68.5	71	749
	A3	C3 (x=625 $\mu\text{m}$ , z=1250 $\mu\text{m}$ )	70.2	214	260
	A4	C4 (x=1250 $\mu\text{m}$ , z=1250 $\mu\text{m}$ )	69.1	68	576
			Mean: 69.8	Mean: 129.0	Mean: 441.0
			St. Dev.: 1.3	St. Dev.: 71.8	St. Dev.: 267.4

957

958 Table 5. Morphological REA size estimates by statistical approach (n=1; error ranging between 5 and 10%). The results of inverse regression and  
959 integral range are also given.

Shale	Statistical morphological REA		
	Regression $\frac{D_{\varphi}^2(S)}{\bar{\varphi}(1-\bar{\varphi})} = \frac{A_2}{S}$	Integral range $A_2$	REA size estimates ( $\mu\text{m}$ ) ( $\varepsilon \in [5,10]\%$ )
Callovo-Oxfordian claystone	$\frac{D_{\varphi}^2(S)}{\bar{\varphi}(1-\bar{\varphi})} = \frac{106.6}{S}$ $R^2 = 0.96$	106.6	205-410
Tournemire argillite	$\frac{D_{\varphi}^2(S)}{\bar{\varphi}(1-\bar{\varphi})} = \frac{703}{S}$ $R^2 = 0.36$	703	345-696

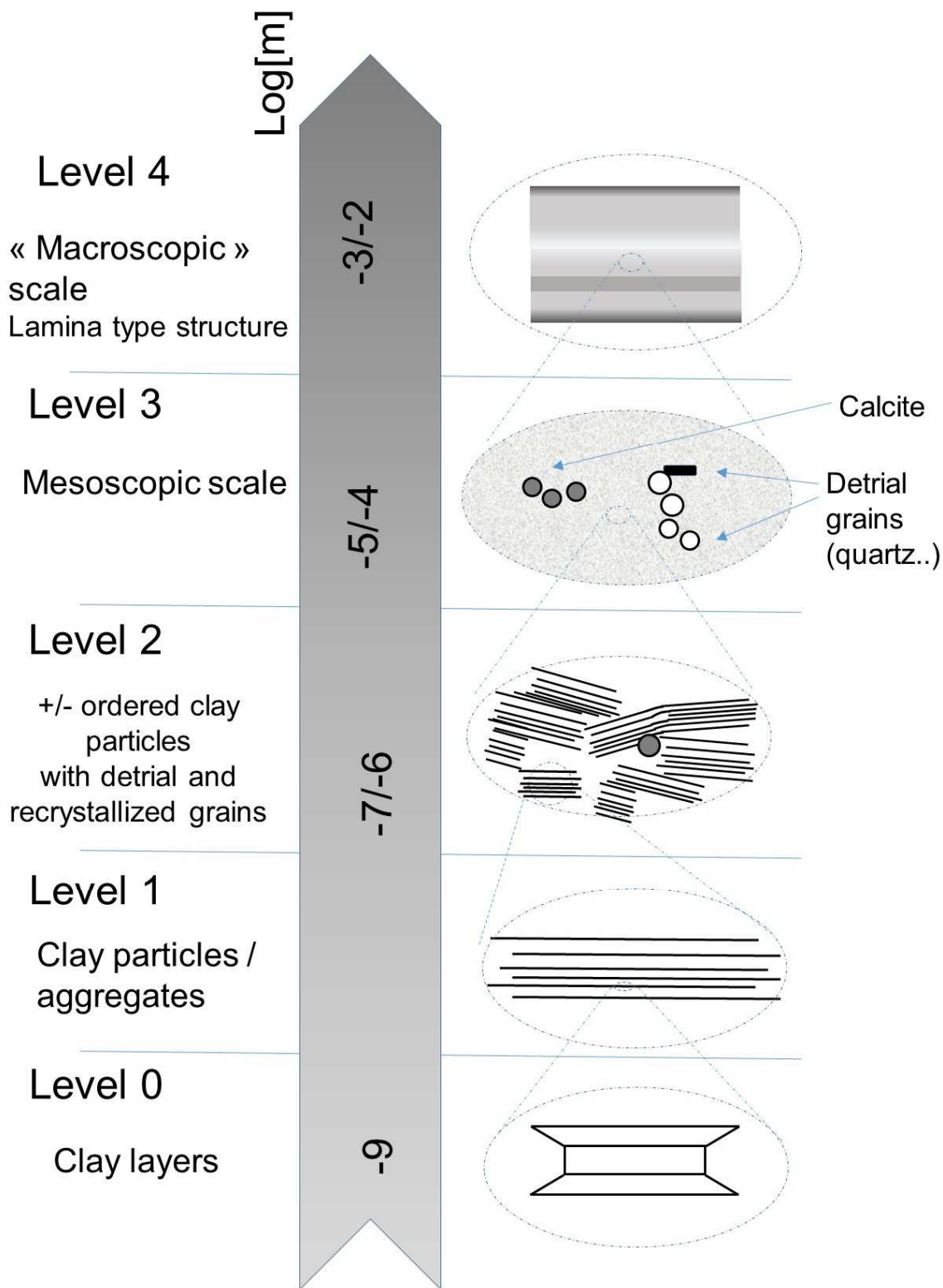
960

961 Table 6. Recapitulation of mechanical REA size estimates by statistical approach (n=1; error ranging between 5 and 10%).

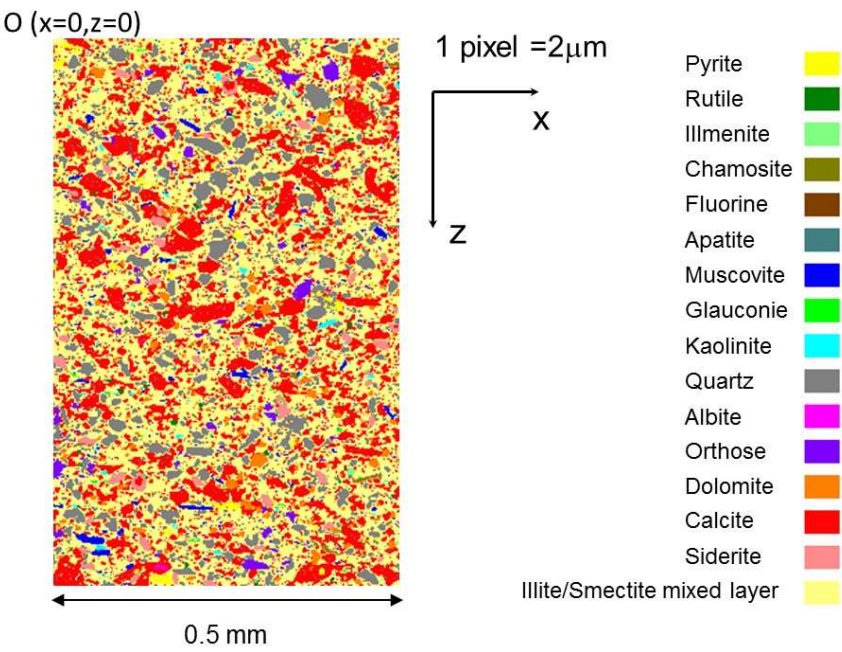
Shale	Statistical mechanical REA							
	Anisotropic model				Isotropic model			
	Bulk modulus		Shear modulus		Bulk modulus		Shear modulus	
	Integral range $A_2$	REA size estimates ( $\mu\text{m}$ ) $\varepsilon \in [5,10]\%$	Integral range $A_2$	REA size estimates ( $\mu\text{m}$ ) $\varepsilon \in [5,10]\%$	Integral range $A_2$	REA size estimates ( $\mu\text{m}$ ) $\varepsilon \in [5,10]\%$	Integral range $A_2$	REA size estimates ( $\mu\text{m}$ ) $\varepsilon \in [5,10]\%$
Callovo-Oxfordian claystone	27.5	353-765	27.7	574-1251	28.2	253-512	29.4	338-664
Tournemire argillite	37.4	743-1759	37.9	748-1772	38.4	687-1594	38.3	720-1688

962

Figure 1. Microstructure of clay-rocks at various scales (modified from Ulm et al. 2005; Sarout and Guéguen, 2008; Cosenza et al., 2015a).



968

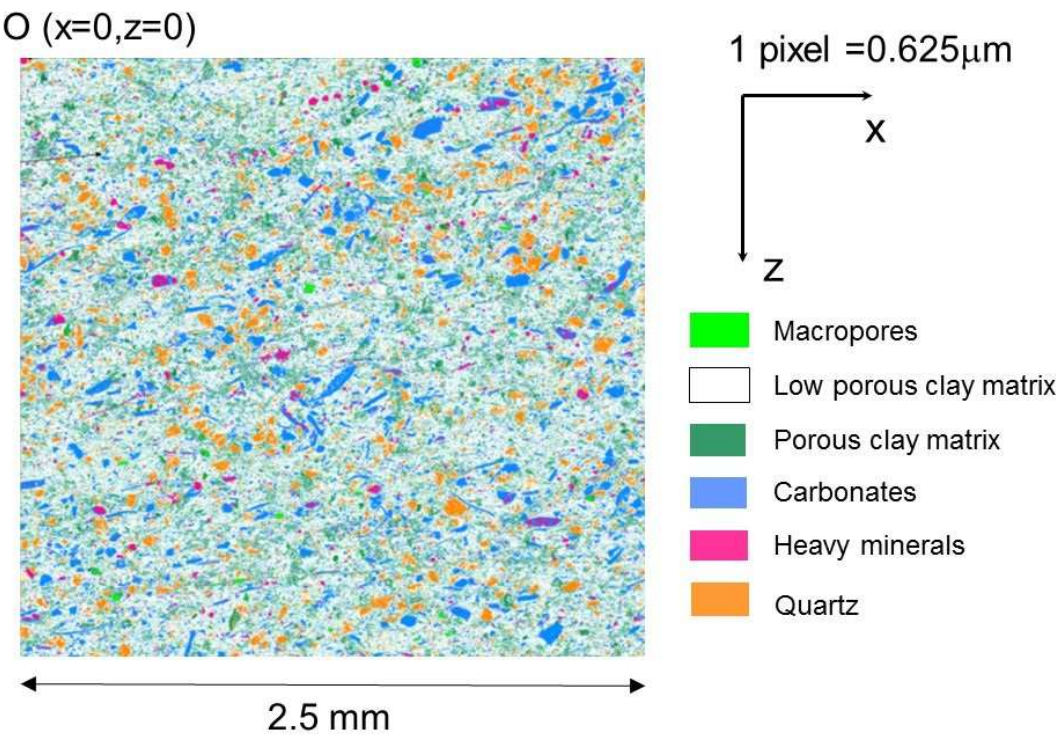


969

970

971

Figure 2. Extraction of the mineral COx map used in this work (modified from Jorand, 2006).

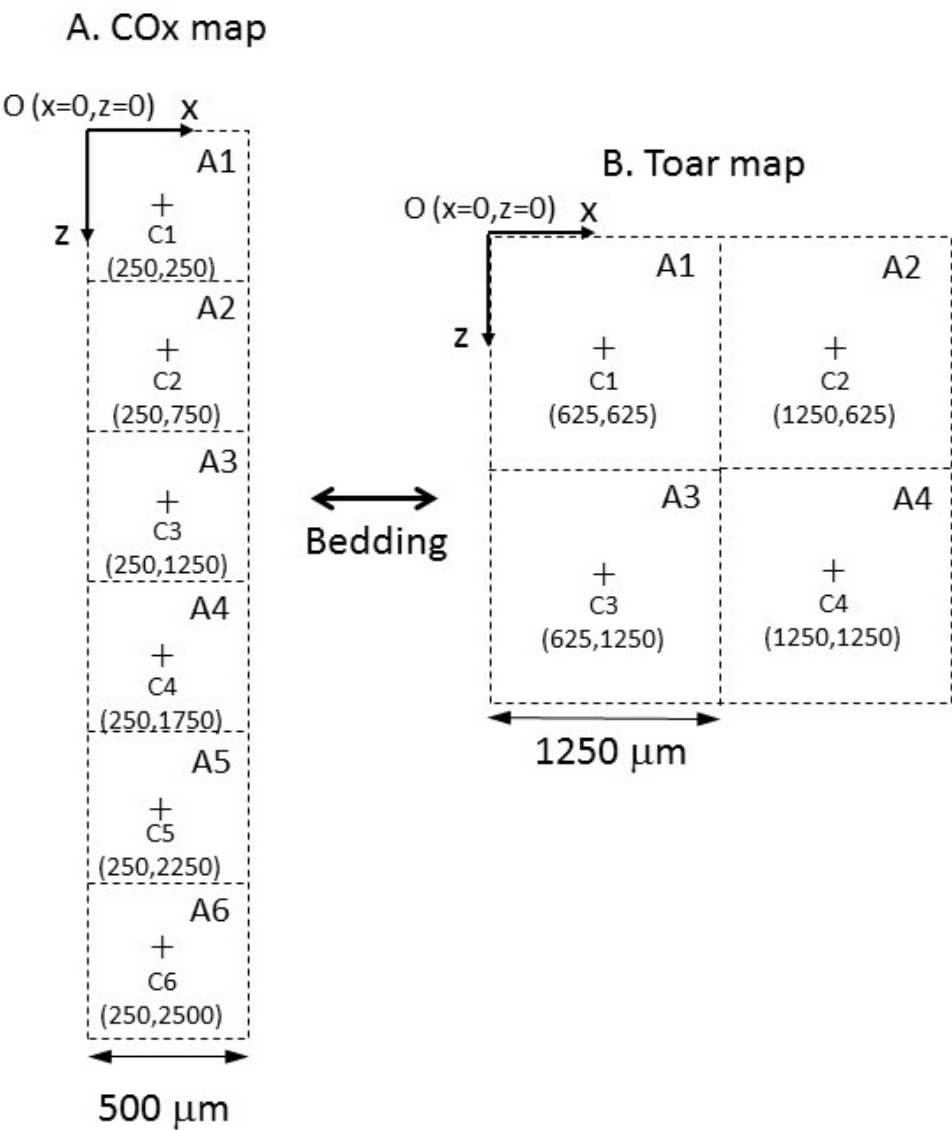


972

973

974

Figure 3. The mineral Toar map used in this work (modified from Fauchille, 2015).



976

977

978

979

980

981

Figure 4. A. Partitioning of the COx map only used for counting box method. B. Partitioning of the Toar map used for counting box method. In both cases, the direction of bedding is indicated.



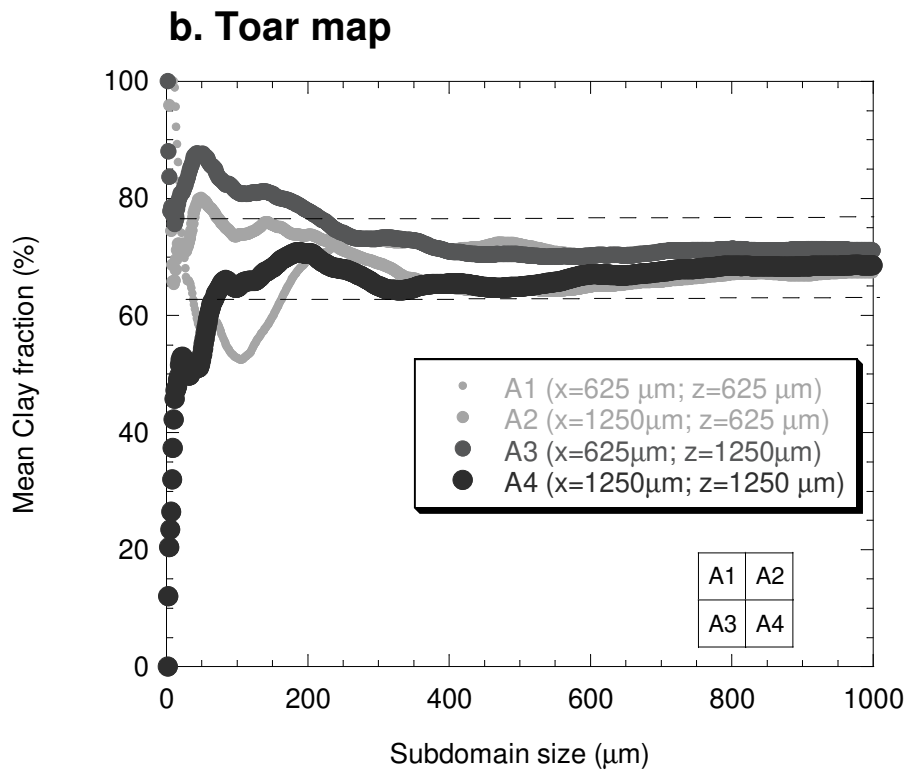
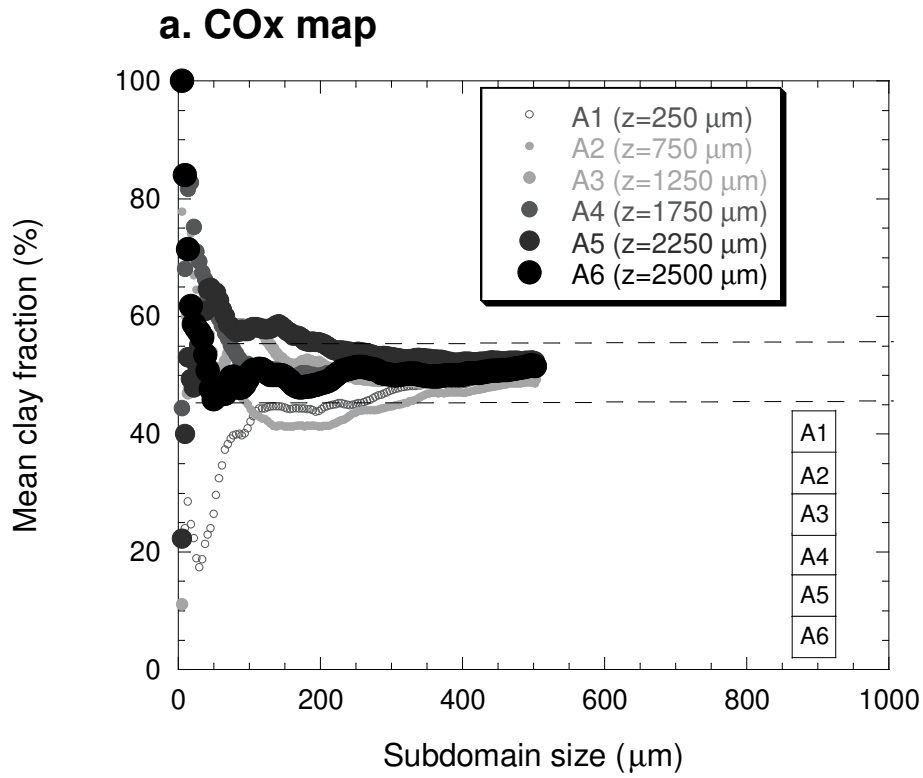


Figure 5. Estimation of the Representative Elementary Area (REA) size of mineral maps by counting box method. Evolution of mean clay fraction with increasing subdomain size (box) and for different starting domains. The coordinates of starting domains are given in the captions boxes (see the origin of the system of Cartesian coordinates in Figures 2 and 3).

989 a. COx map. The x-coordinates of the starting domains is 250  $\mu\text{m}$ . The horizontal dashed lines  
990 indicate the range of mean clay fraction corresponding to  $(1 \pm \varepsilon)\bar{\phi}_{\text{COx}}$  with  $\bar{\phi}_{\text{COx}}=0.504$   
991 (50.4%) and  $\varepsilon=0.1(10\%)$ .  
992 b. Toar map. The horizontal dashed lines indicate the range [62.9-76.9%] corresponding to  
993  $(1 \pm \varepsilon)\bar{\phi}_{\text{Toar}}$  with  $\bar{\phi}_{\text{Toar}}=0.699$  (69.9%) and  $\varepsilon=0.1(10\%)$ .  
994  
995

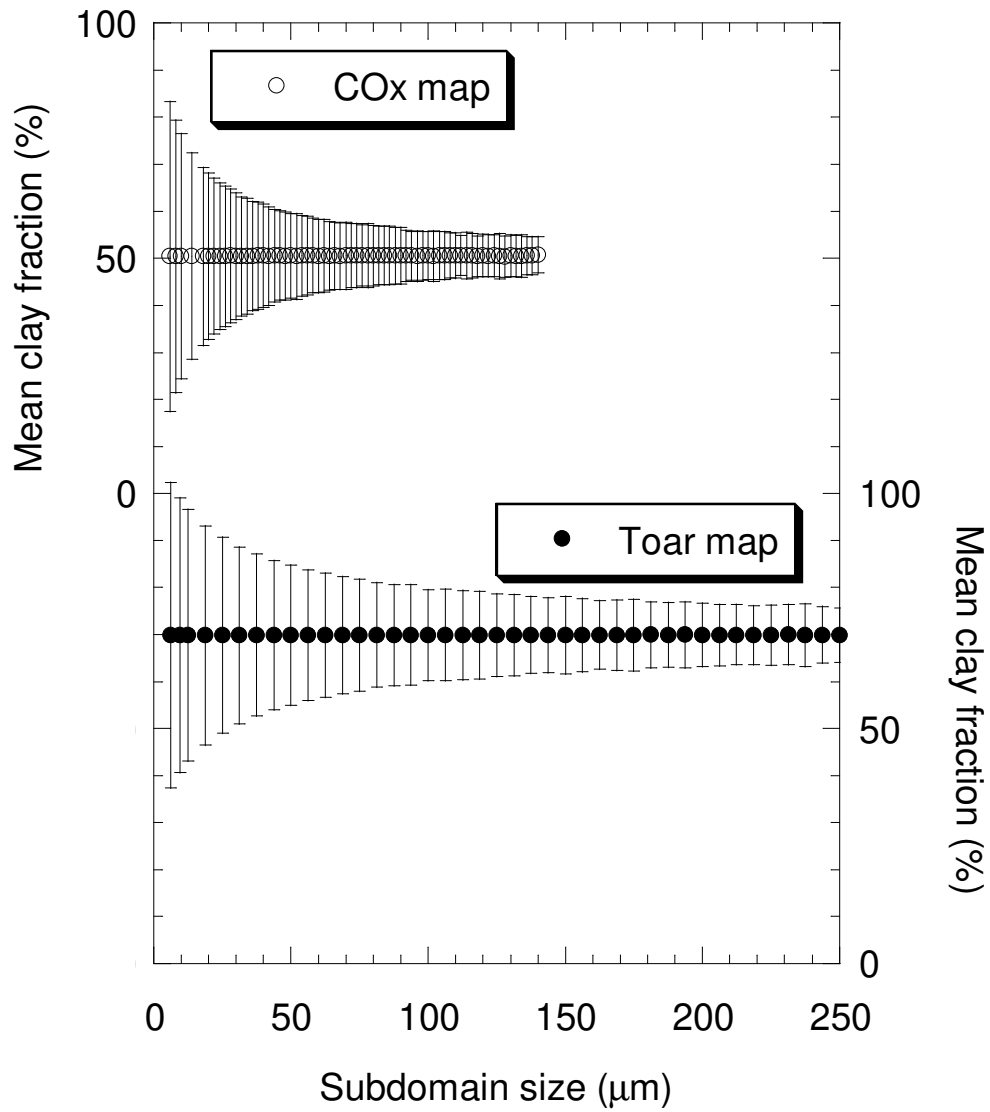
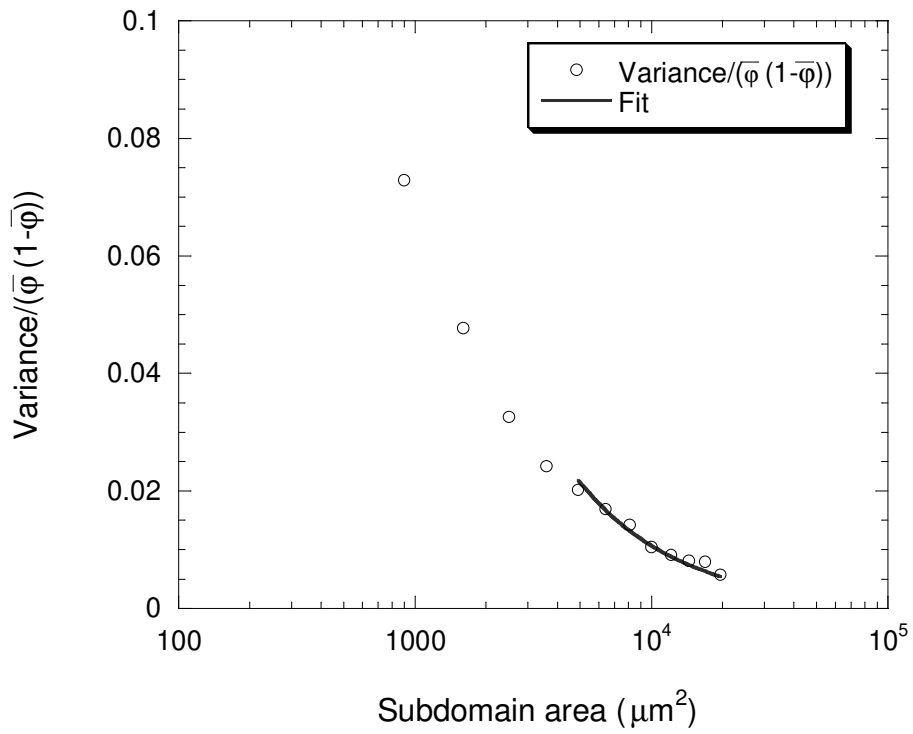


Figure 6. Evolution of the mean clay fraction and related standard deviation versus the subdomain size  $L$  for both maps.

### a. COx map



### b. Toar map

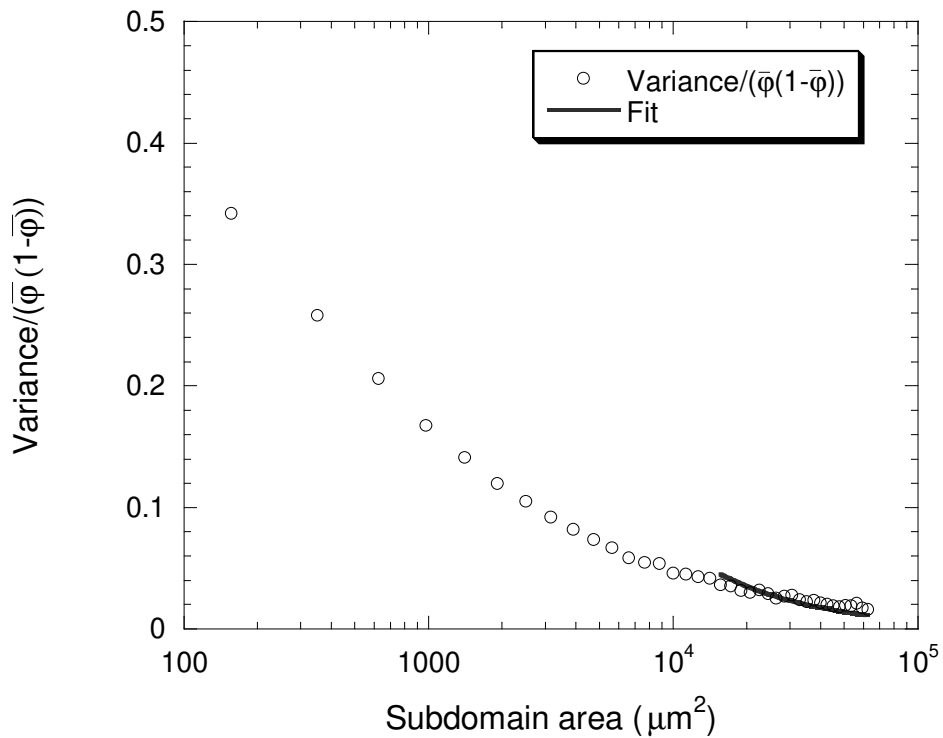
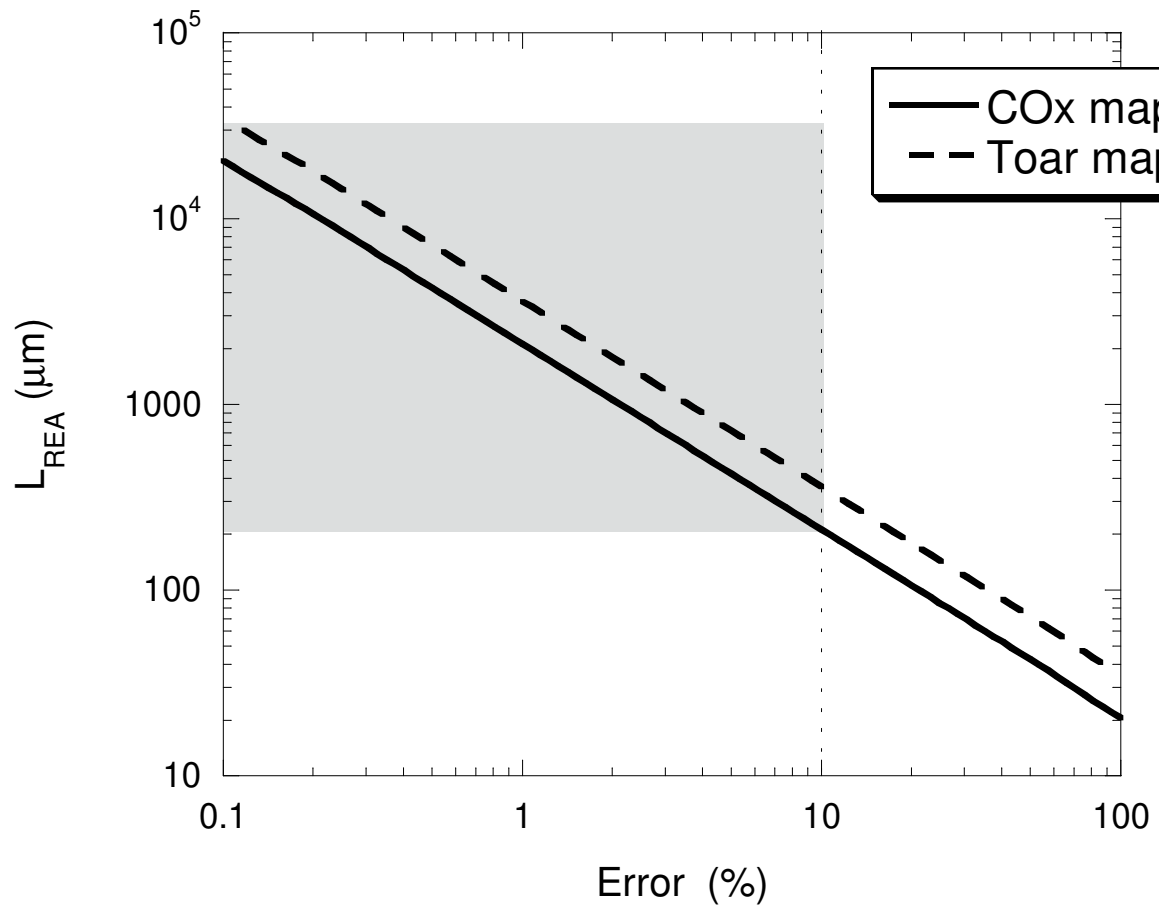


Figure 7. Determination of the “morphological” integral range  $A_2$ . Evolution of the pseudovariance of the clay fraction, i.e.,  $\text{Variance}(\bar{\varphi}_{arg}(1-\bar{\varphi}_{arg}))$  as a function of  $1/S$ , where  $S$  is the box size area. A linear fit is indicated by a bold line. a. COx map. b. Toar map.



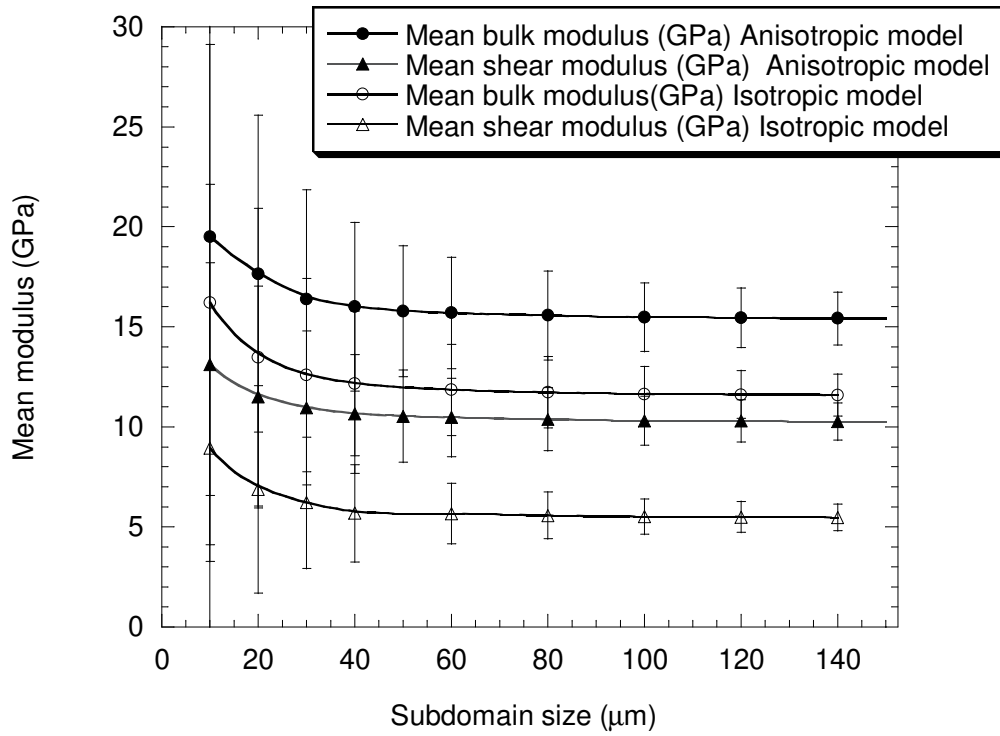
1006

1007 Figure 8. Morphological REA size, L<sub>REA</sub> (μm) as a function of error (%) for one realization

1008 (n=1) for both mineral maps.

1009

### a. COx map



### b. Toar map

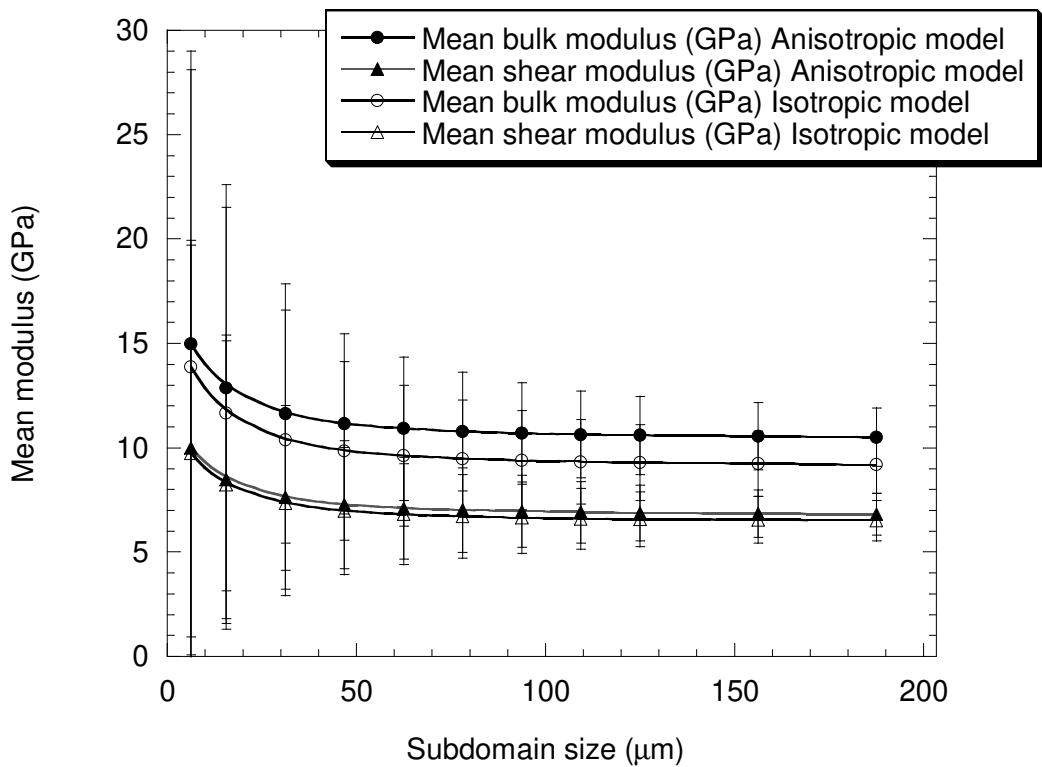


Figure 9. Mean value and dispersion (standard deviation) of the apparent elastic moduli as a function of the subdomain size  $L$  in the case of the anisotropic model and isotropic model. a: COx map. b: Toar map.

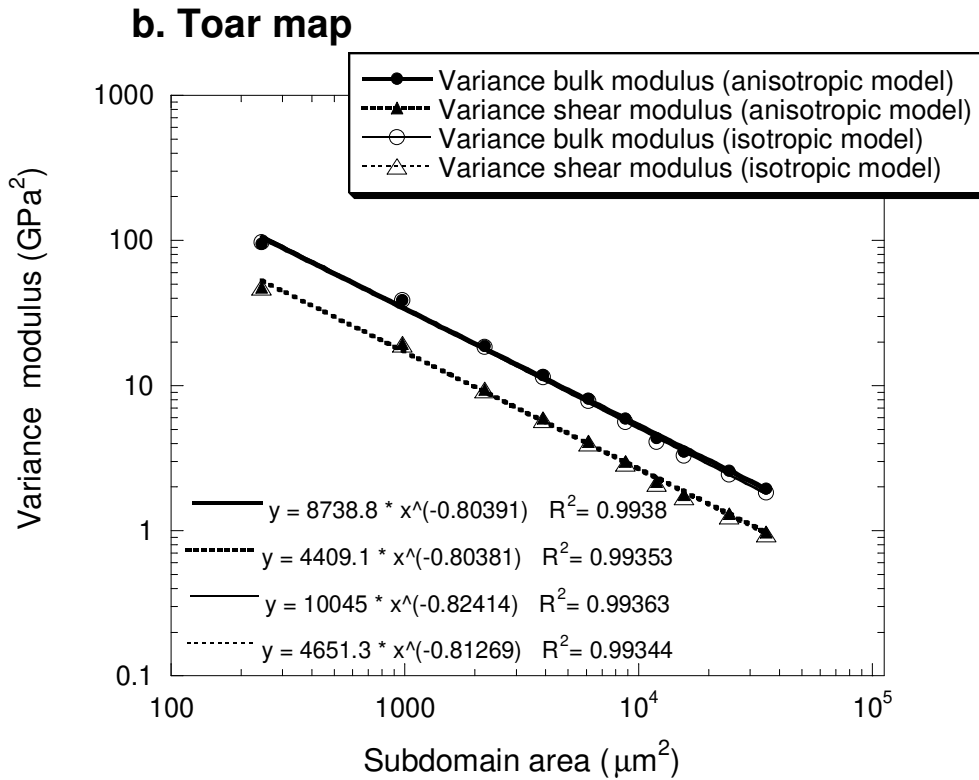
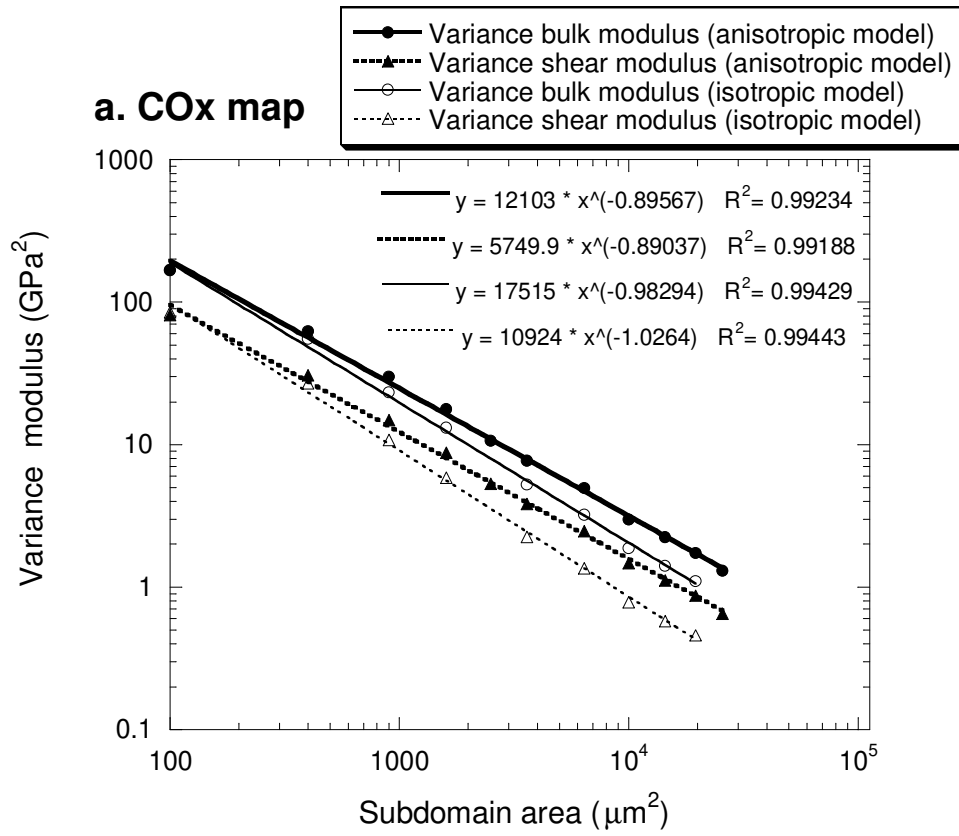


Figure 10. Determination of the “mechanical” integral range  $A_2$ . Evolution of the variance of the elastic modulus of the anisotropic and isotropic models as a function of the subdomain area. Power fits are also indicated to calculate the integral range values. a. COx map. b. Toar map.

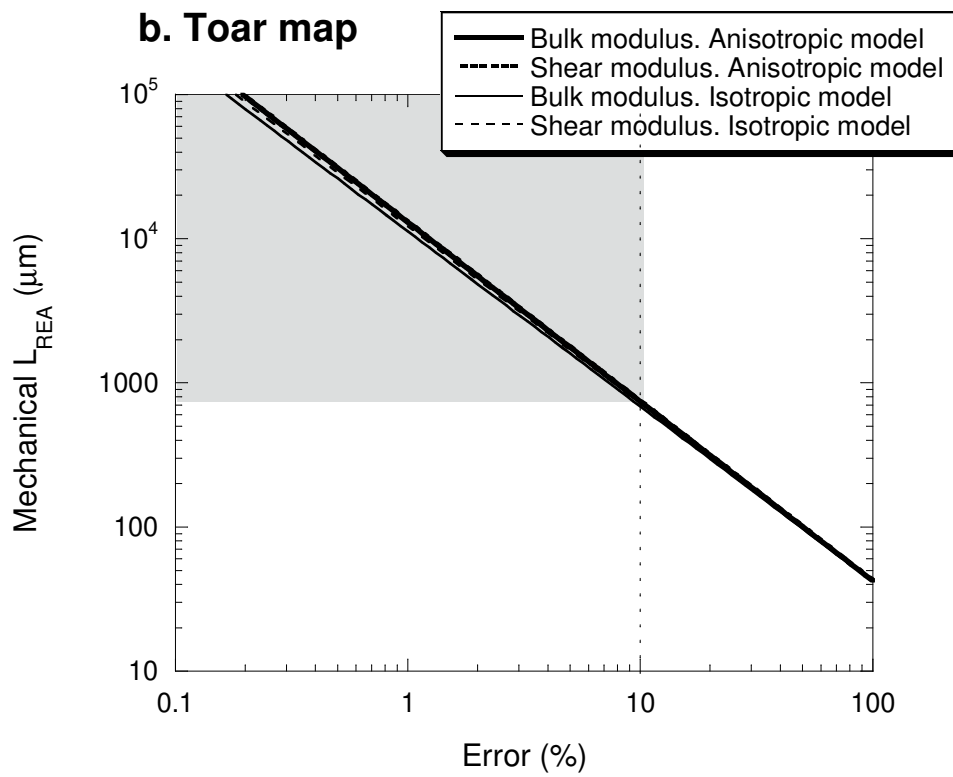
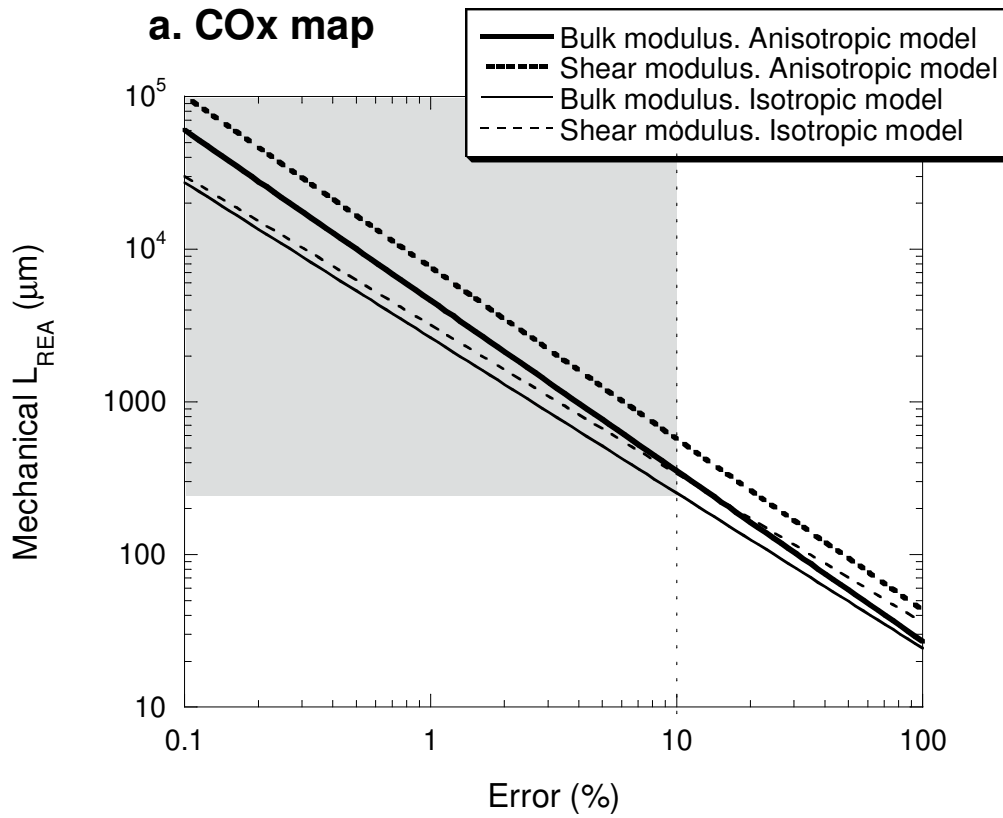


Figure 11. Mechanical REA size,  $L_{\text{REA}}$  ( $\mu\text{m}$ ), as a function of error (%) for one realization ( $n=1$ ). Both elastic moduli, i.e., the bulk modulus and shear modulus; both micromechanical models, i.e., the anisotropic model and isotropic model, are considered. a. COx map. b. Toar map.



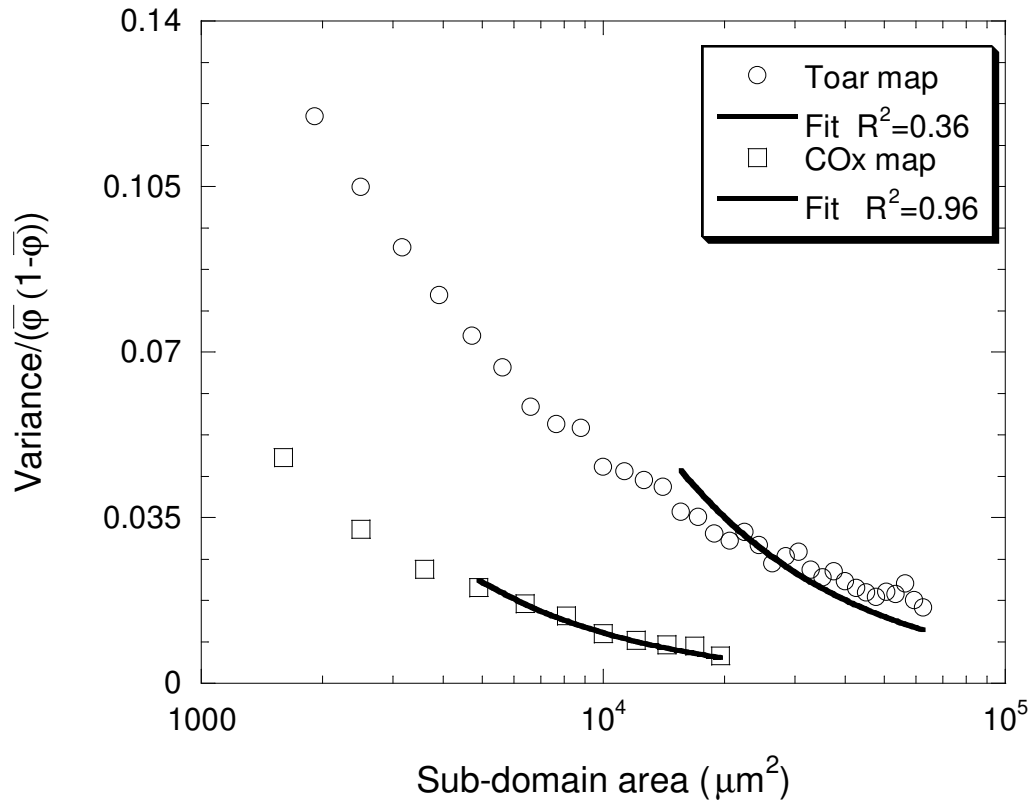


Figure 12. Zoom of the evolutions of the pseudo-variance of clay fraction i.e.,  $\text{Variance}(\bar{\varphi}_{arg}(1-\bar{\varphi}_{arg}))$  as a function of subdomain area of both maps.  $R^2$  values of both fits are also given.